Molecular Cell

Article

Unconventional initiation of PINK1/Parkin mitophagy by Optineurin

Graphical abstract

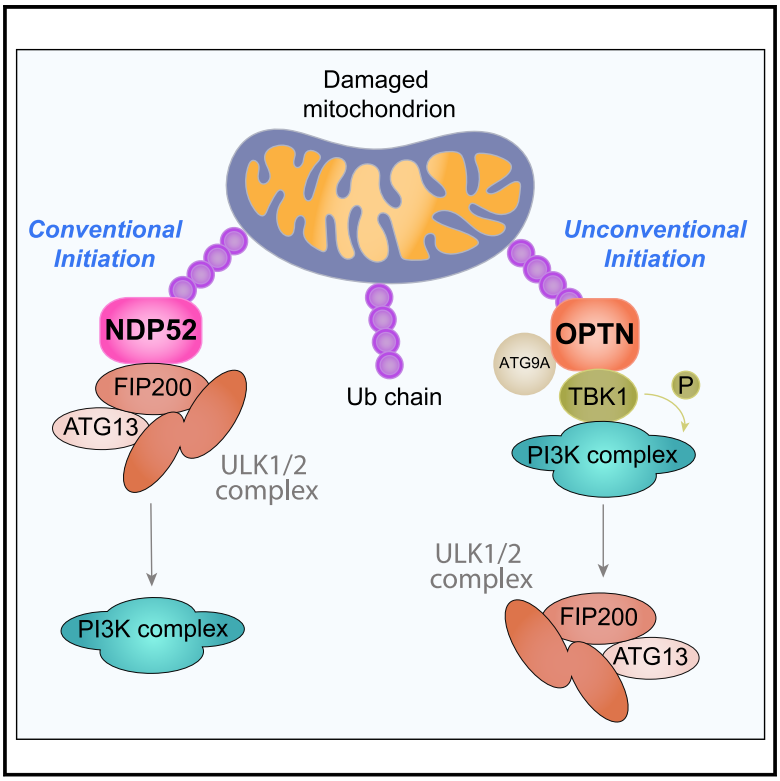

Highlights

- OPTN and NDP52 are mechanistically distinct autophagy adaptors
- OPTN uses TBK1, but not ULK1/2, to initiate mitophagy
- TBK1 directly binds and phosphorylates the PI3K complex
- TBK1 can function as a ULK1/2-like kinase in selective autophagy initiation

Authors

Thanh Ngoc Nguyen, Justyna Sawa-Makarska, Grace Khuu, ..., Runa S.J. Lindblom, Sascha Martens, Michael Lazarou

Correspondence

lazarou.m@wehi.edu.au (M.L.), sascha.martens@univie.ac.at (S.M.), nguyen.tha@wehi.edu.au (T.N.N.)

In brief

Nguyen et al. discover an unconventional mechanism by which Optineurin drives mitophagy initiation and by doing so reveal the mechanistic plasticity in how selective autophagy can be initiated. They also classify TBK1 as a selective autophagy-initiating kinase that can function in an ULK1/2-like fashion to recruit the PI3K complex.

Nguyen et al., 2023, Molecular Cell *83*, 1693–1709
May 18, 2023
https://doi.org/10.1016/j.molcel.2023.04.021

CellPress

Molecular Cell

CellPress
OPEN ACCESS

Article

Unconventional initiation of PINK1/Parkin mitophagy by Optineurin

Thanh Ngoc Nguyen,[1,2,3,4,*] Justyna Sawa-Makarska,[4,5] Grace Khuu,[1,2,3,4] Wai Kit Lam,[1,2,3,4] Elias Adriaenssens,[4,5] Dorotea Fracchiolla,[4,5,6] Stephen Shoebridge,[4,5] Daniel Bernklau,[4,5] Benjamin Scott Padman,[3,4,7] Marvin Skulsuppaisarn,[1,2,3] Runa S.J. Lindblom,[1,2,3,4] Sascha Martens,[4,5,*] and Michael Lazarou[1,2,3,4,8,*]

[1]Walter and Eliza Hall Institute of Medical Research, Parkville, Victoria, Australia
[2]Department of Medical Biology, University of Melbourne, Melbourne, Victoria, Australia
[3]Department of Biochemistry and Molecular Biology, Biomedicine Discovery Institute, Monash University, Melbourne, Australia
[4]Aligning Science Across Parkinson's (ASAP) Collaborative Research Network, Chevy Chase, MD 20815, USA
[5]Department of Biochemistry and Cell Biology, Max Perutz Labs, University of Vienna, Vienna BioCenter, Dr. Bohr-Gasse 9, 1030 Vienna, Austria
[6]Present address: Department of Theoretical Biophysics, Max Planck Institute of Biophysics, Frankfurt am Main, Germany
[7]Present address: Center for Microscopy, Characterization and Analysis, University of Western Australia, Perth, 6009 Australia
[8]Lead contact
*Correspondence: lazarou.m@wehi.edu.au (M.L.), sascha.martens@univie.ac.at (S.M.), nguyen.tha@wehi.edu.au (T.N.N.)
https://doi.org/10.1016/j.molcel.2023.04.021

SUMMARY

Cargo sequestration is a fundamental step of selective autophagy in which cells generate a double-membrane structure termed an "autophagosome" on the surface of cargoes. NDP52, TAX1BP1, and p62 bind FIP200, which recruits the ULK1/2 complex to initiate autophagosome formation on cargoes. How OPTN initiates autophagosome formation during selective autophagy remains unknown despite its importance in neurodegeneration. Here, we uncover an unconventional path of PINK1/Parkin mitophagy initiation by OPTN that does not begin with FIP200 binding or require the ULK1/2 kinases. Using gene-edited cell lines and *in vitro* reconstitutions, we show that OPTN utilizes the kinase TBK1, which binds directly to the class III phosphatidylinositol 3-kinase complex I to initiate mitophagy. During NDP52 mitophagy initiation, TBK1 is functionally redundant with ULK1/2, classifying TBK1's role as a selective autophagy-initiating kinase. Overall, this work reveals that OPTN mitophagy initiation is mechanistically distinct and highlights the mechanistic plasticity of selective autophagy pathways.

INTRODUCTION

Macroautophagy (hereafter autophagy) is a highly conserved catabolic process that degrades and recycles intracellular components. Autophagy is cytoprotective and plays essential roles in maintaining cellular homeostasis through the removal of harmful materials such as protein aggregates, dysfunctional organelles, and invading pathogens.[1,2] Cargoes destined for autophagic degradation are sequestered by double-membrane vesicles termed autophagosomes before being delivered to lysosomes for degradation. Autophagosomes are generated through the formation of a double-membrane precursor termed the phagophore that arises on a platform of endoplasmic reticulum termed the omegasome.[3–5]

A general hierarchy of autophagy machinery recruitment during autophagosome formation has been established and typically begins with concurrent recruitment of ATG9A vesicles and the ULK1/2 complex, the latter consisting of the kinase ULK1 or its homolog ULK2, FIP200, ATG13, and ATG101.[1,2,6–9] The ULK1/2 complex then promotes the recruitment and activation of the class III phosphatidylinositol 3-kinase complex I (hereafter PI3K complex). The PI3K complex consists of ATG14, the lipid kinase VPS34, VPS15, and Beclin, which together function to generate the lipid phosphatidylinositol 3-phosphate (PI(3)P) on phagophore membranes. This enables the recruitment of PI(3)P effector proteins including the WIPIs (WD-repeat protein interacting with phosphoinositides) that promote phagophore expansion. WIPI2 plays a role in recruiting the ATG8 conjugation machinery through binding to the ATG16L1 subunit,[10] resulting in the attachment of ubiquitin-like ATG8 family proteins onto phosphatidylethanolamine (PE) on autophagosomal membranes.[11,12] The similarity of ATG8 conjugation to ubiquitination has led to the process being termed atg8ylation, which describes the conjugation of ATG8s to lipid or protein.[13–16] The ATG8 family consists of six members divided equally across the LC3 and GABARAP subfamilies. Attachment of ATG8s to PE may function to expand autophagosomal membranes, at least in part, via promoting membrane tethering and hemifusion[17] and by acting as a protein platform to recruit autophagy factors.[18,19] WIPI1 and WIPI4 can function to promote

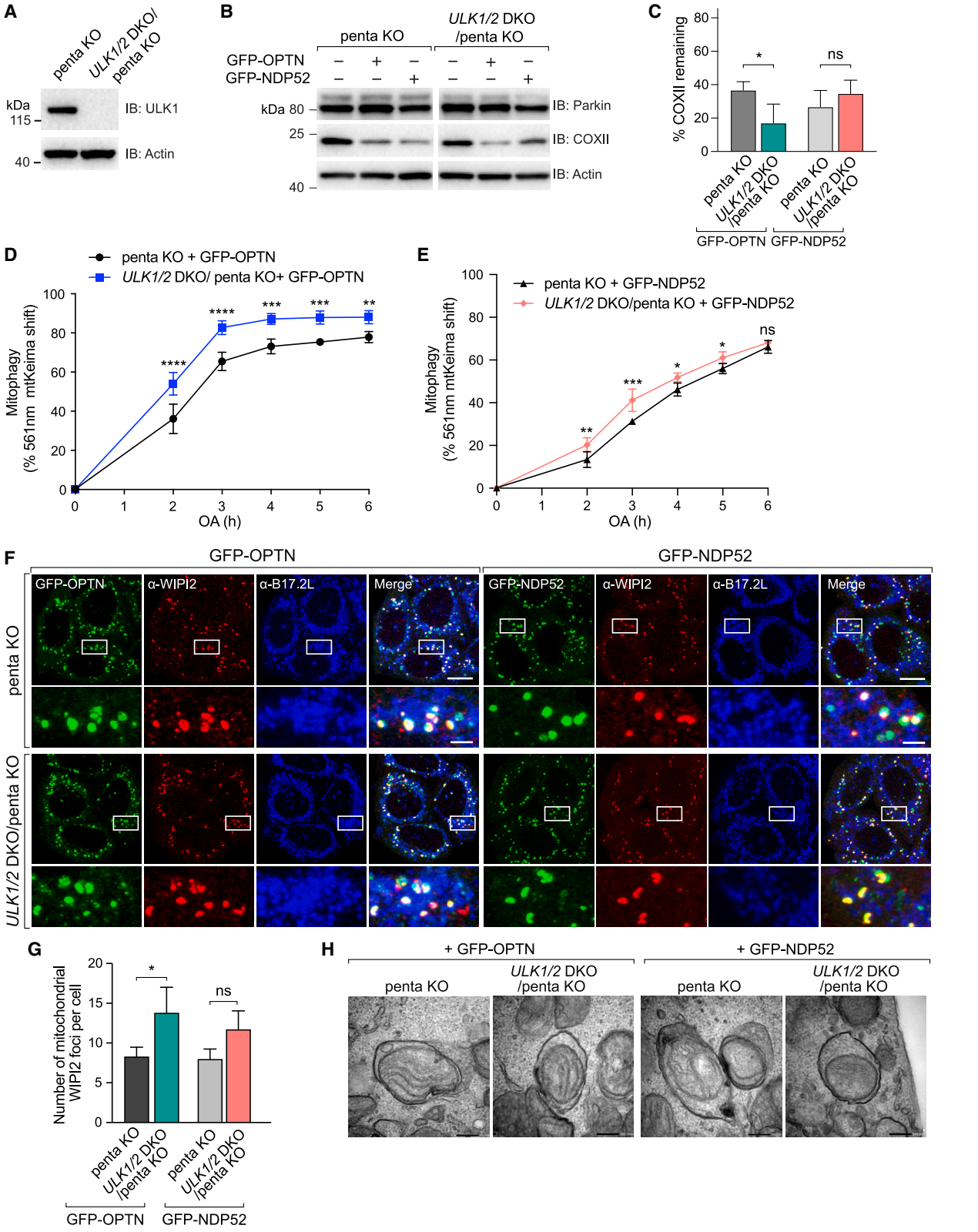

(legend on next page)

membrane expansion through their interactions with ATG2 proteins that transfer phospholipids from the ER to the growing phagophore.[20–25] ATG9A facilitates ATG2-mediated lipid transfer by enabling ER-phagophore contacts and acting as a lipid scramblase by re-arranging lipids from the cytoplasmic leaflet to the luminal leaflet of the growing phagophore.[26–29] ATG9A vesicles, which are trafficked to autophagosome formation sites by ARFIP2, the immune disease protein LRBA, and the ATG4 family,[15,30] might also provide the membrane seed for initial phagophore formation.[30–33]

Selective targeting of autophagic cargoes, including the ER, invading pathogens, and mitochondria, necessitates the recruitment of autophagy machineries to the surface of cargo to enable selective capture by autophagosomes. Selective recruitment of autophagy machineries is conducted by receptor proteins resident on the surface of cargoes or via adaptor proteins that recognize "eat me" signals on the surface of cargo in the form of ubiquitin chains.[34–36] Several autophagy adaptors have been identified and among the most highly studied are p62, NBR1, NDP52, TAX1BP1, and optineurin (OPTN).[19] These autophagy adaptors appear to use a common mechanism of engaging the autophagy machinery by recruiting the ULK1/2 complex through binding to the FIP200 subunit to initiate the cascade of autophagosome formation.[37–40] In addition to the ULK1 and ULK2 kinases, TBK1 is another kinase that has been linked to selective autophagy pathways,[37,41–45] although its precise role during selective autophagy driven by each individual autophagy adaptor remains unclear.

Defects in selective autophagy have been linked to disease in humans, including neurodegeneration in Parkinson's disease which has been associated with defects in PINK1/Parkin mitophagy.[1,46] The kinase PINK1 and the ubiquitin ligase Parkin are mutated in familial Parkinson's disease[47,48] and together function to drive mitophagy of damaged and dysfunctional mitochondria.[49–54] PINK1 and Parkin generate ubiquitin chains on the mitochondrial outer membrane that recruit the primary mitophagy adaptor proteins, OPTN and NDP52[41,42,55] to initiate autophagosome formation on damaged mitochondria.[37,41] OPTN and NDP52 are also recruited downstream of autophagosome initiation by ATG8s via an LC3 interacting region (LIR) motif to amplify mitophagy.[56] To initiate PINK1/Parkin mitophagy, NDP52 directly binds to the FIP200 subunit of the ULK1/2 complex to trigger autophagosome biogenesis.[37,38] TBK1 functions to phosphorylate NDP52 and OPTN to increase their affinity for ubiquitin chains and ATG8s[42,43,57] and also to promote NDP52-FIP200 interactions to drive efficient mitophagy.[37] In addition, TBK1 coordinates with OPTN for efficient sequestration of damaged mitochondria.[45,55,58] However, the mechanism behind how OPTN initiates autophagosome formation during PINK1/Parkin mitophagy remains unclear. A recent *in vitro* study reported the structure of FIP200's Claw domain bound to the TBK1-phosphorylated LIR domain of OPTN,[59] indicating that OPTN may potentially use the same mechanism as NDP52 to initiate PINK1/Parkin mitophagy. Another study reported that an OPTN-ATG9A interaction, which is independent of TBK1, is crucial for PINK1/Parkin mitophagy.[60] However, it is unclear if this interaction regulates autophagosome initiation or other downstream steps since ATG9A seems to be involved in multiple stages during autophagosome biogenesis.[61] Nevertheless, for autophagy adaptors, the conventional path of selective autophagy initiation identified to date involves direct interaction with FIP200, as has been reported for NDP52 during mitophagy and xenophagy,[37,38] and for p62 and TAX1BP1 during aggrephagy.[39,40]

OPTN is mutated in human neurodegenerative diseases including amyotrophic lateral sclerosis (ALS) and glaucoma,[62,63] and unlike NDP52, OPTN is highly expressed in brain tissue,[41] making it a high-priority cargo adaptor to understand. In this study, we uncover OPTN's mechanism for initiating selective autophagy. Our work shows that OPTN follows an unconventional path by utilizing TBK1 to interact with the PI3K complex upstream of ULK1/2 complex recruitment. The ULK1/2 kinase subunits were found to be dispensable for OPTN-mediated mitophagy but can contribute to NDP52-mediated mitophagy in a functionally redundant manner with TBK1, revealing TBK1 as a ULK1/2-like kinase in mitophagy. These results demonstrate the mechanistic divergence of mitophagy initiation by OPTN from NDP52 and other cargo adaptors, revealing an alternative path of selective autophagy initiation.

RESULTS

ULK1 and ULK2 are dispensable for PINK1/Parkin mitophagy

ULK1 has been reported to phosphorylate several autophagy factors that are important for autophagosome formation.[64–66] Given the role of ULK1 and its relative ULK2 as the most upstream kinases of autophagy, we assessed their contribution to PINK1/Parkin mitophagy initiation mediated by either OPTN or NDP52. Knockouts (KOs) of ULK1 and ULK2 were conducted in the HeLa penta KO background that lacks the five autophagy adaptors OPTN, NDP52, TAX1BP1, NBR1, and p62 (Figure 1A)

Figure 1. ULK1 and ULK2 are dispensable for Pink1/Parkin mitophagy

(A) *ULK1/2* DKO in penta KO background was confirmed by immunoblotting (IB). kDa, kilodaltons.

(B and C) penta KO and *ULK1/2* DKO/penta KO expressing BFP-Parkin and GFP-OPTN or GFP-NDP52 were treated with OA for 18 h and analyzed by immunoblotting (B) and COXII levels were quantified (C).

(D and E) penta KO and *ULK1/2* DKO/penta KO cells expressing BFP-Parkin, mtKeima, and GFP-OPTN (D) or GFP-NDP52 (E) untreated or treated with OA for indicated times were analyzed by FACS. Lysosomal-positive mtKeima was calculated as the percentage of 561 nm mtKeima-positive cells. Representative FACS blots are provided in Figure S1A.

(F and G) penta KO and *ULK1/2* DKO/penta KO cells expressing BFP-Parkin and GFP-OPTN or GFP-NDP52 were treated with OA for 1 h and immunostained for WIPI2 and B17.2L (F) and the number of mitochondrial WIPI2 puncta per cell was quantified (G). Untreated samples shown in Figure S1B.

(H) penta KO and *ULK1/2* DKO/penta KO expressing BFP-Parkin and GFP-OPTN or GFP-NDP52 were treated with OA and BafA1 for 3 h and subjected to transmission EM (TEM). Data in (C)–(E) and (G) are mean ± SD from three independent experiments. *$p < 0.05$, **$p < 0.005$, ***$p < 0.001$, ****$p < 0.0001$ (E, G one-way analysis of variance [ANOVA]; C, D two-way ANOVA). ns, not significant. Scale bars, (F) overviews, 10 μm; insets, 2 μm; (H) 200 nm.

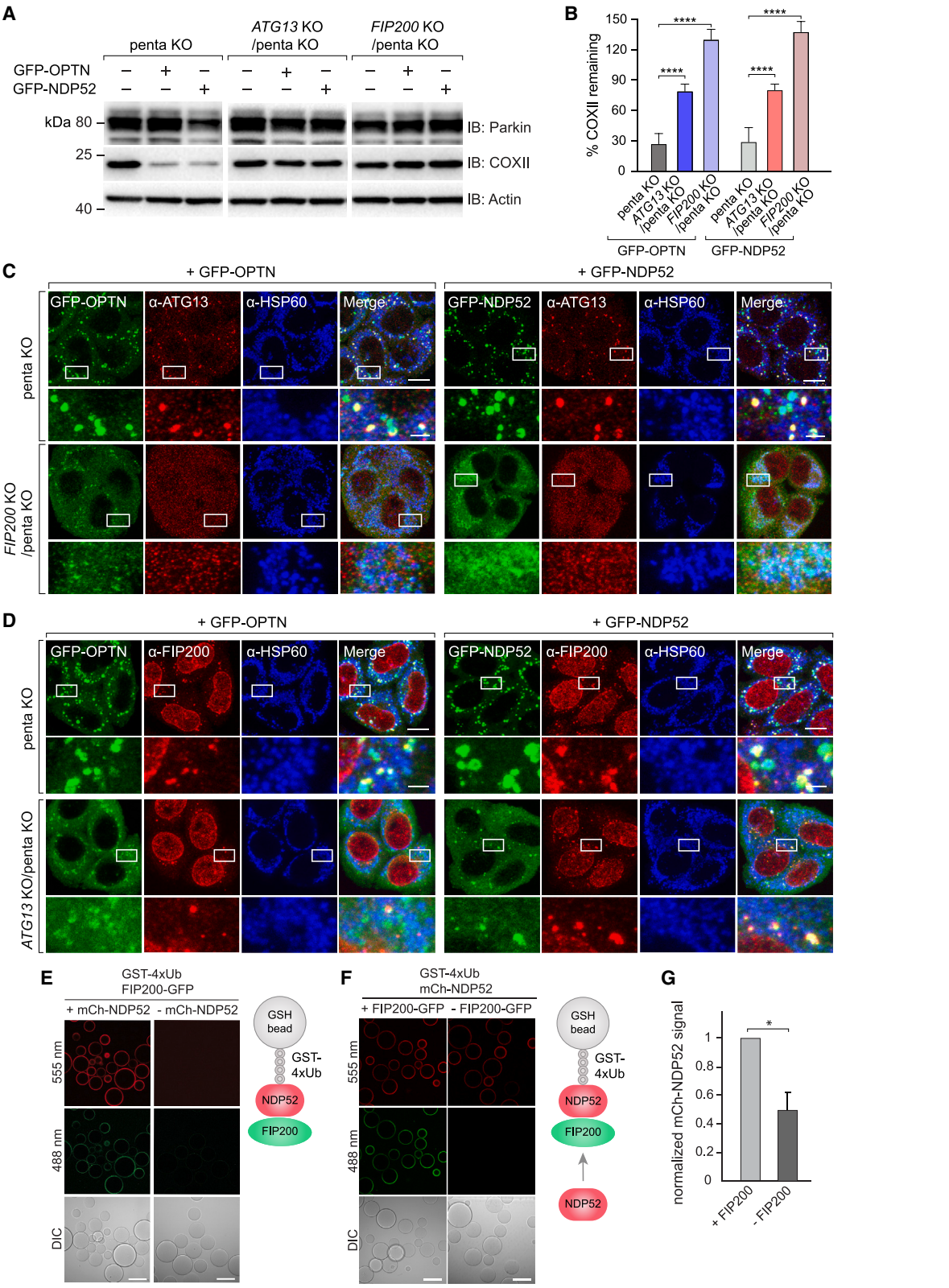

(legend on next page)

to enable individual assessment of OPTN- or NDP52-mediated PINK1/Parkin mitophagy. Mitophagy was induced by treating cells with Oligomycin and Antimycin A (OA) and assessed by measuring the degradation of cytochrome *c* oxidase subunit II (COXII), a mitochondrial DNA-encoded protein located within the inner membrane. As can be seen in Figures 1B and 1C, the loss of ULK1/2 did not prevent COXII degradation in GFP-NDP52 expressing *ULK1/2* DKO/penta KO cells (DKO: double knockout), and even slightly increased the levels of COXII degradation in GFP-OPTN expressing cells. To determine if the efficiency of mitophagy was affected in the absence of ULK1/2, the mtKeima mitophagy assay was employed.[37,41,67] Consistent with the COXII degradation data in Figures 1B and 1C, there was no mitophagy defect in penta KO cells lacking ULK1/2 undergoing either GFP-OPTN or GFP-NDP52 driven mitophagy (Figures 1D and 1E). Instead, mitophagy rates appeared to be slightly higher for GFP-OPTN mitophagy (Figure 1D), and to a lesser degree the same was true for GFP-NDP52 (Figure 1E). Analysis of mitochondrial recruitment of the early autophagosome marker WIPI2b showed that the loss of ULK1/2 did not decrease the formation of autophagosome precursors (Figures 1F and 1G). Consistent with the mitophagy measurements in Figures 1D and 1E, the loss of ULK1/2 resulted in a more robust formation of WIPI2b autophagosome intermediates during GFP-OPTN-dependent mitophagy and to a lesser degree during GFP-NDP52-dependent mitophagy (Figures 1F and 1G). Autophagosome formation and overall autophagosome morphology in the absence of ULK1/2 also appeared normal by electron microscopy (EM) analysis (Figure 1H). These results show that despite the role of ULK1 and ULK2 as the most upstream kinases of autophagy, they unexpectedly are not essential for autophagosome formation and mitophagy mediated by either OPTN or NDP52.

The ULK1/2 complex subunits, FIP200 and ATG13, are important for PINK1/Parkin mitophagy

We next asked whether the other subunits of the ULK1/2 kinase complex, including FIP200 and ATG13, are required for PINK1/Parkin mitophagy. Consistent with their essential role in general mammalian autophagy,[68,69] the KO of FIP200 or ATG13 in penta KO cells (Figures S2A and S2B) blocked PINK1/Parkin mitophagy mediated by either GFP-OPTN or GFP-NDP52, as measured by COXII degradation (Figures 2A and 2B). Next, the recruitment of ATG13 and FIP200 foci to mitochondria was analyzed in penta KO cells lacking FIP200 or ATG13, respectively. In the absence of FIP200, neither GFP-OPTN nor GFP-NDP52 could recruit ATG13 foci to mitochondria upon mitophagy induction (Figure 2C). Similarly, in the absence of ATG13, GFP-OPTN could not trigger mitochondrial recruitment of FIP200 foci (Figure 2D). By contrast, GFP-NDP52 was capable of recruiting FIP200 foci to damaged mitochondria in the absence of ATG13 (Figure 2D), which is consistent with the ability of NDP52 to directly bind FIP200.[37,38] These results show that the FIP200 and ATG13 subunits of the ULK1/2 complex are both important for OPTN- and NDP52-dependent PINK1/Parkin mitophagy. Notably, the inability of OPTN to stably recruit FIP200 in the absence of ATG13 indicates that OPTN uses a mechanistically distinct form of mitophagy initiation from NDP52.

In the analyses of GFP-NDP52-mediated recruitment of ATG13 and FIP200 (Figures 2C and 2D), we noted that GFP-NDP52 failed to form mitochondrial foci in the absence of FIP200. This result led us to hypothesize that NDP52-FIP200 interactions can form a positive feedback loop to allow further recruitment and therefore foci formation of NDP52 on damaged mitochondria. We tested this hypothesis by reconstituting NDP52 recruitment *in vitro* using recombinant proteins and a fluorescence microscopy-based bead assay.[70] Recombinant mCherry (mCh)-NDP52 was robustly recruited to cargo mimetic GST-4xUb beads, and this then allowed the recruitment of FIP200-GFP (Figure 2E), providing further confirmation that NDP52 directly interacts with FIP200.[37,38,71] However, in the absence of FIP200, the levels of mCh-NDP52 recruited to the GST-4xUb beads was significantly reduced (Figures 2F and 2G), consistent with the failure to form mitochondrial foci in cells lacking FIP200 (Figure 2C). The presence of FIP200 therefore enhances NDP52 recruitment to cargo, supporting the existence of a FIP200-dependent recruitment loop for NDP52.

TBK1 is essential for OPTN-mediated mitophagy but functions redundantly with ULK1/2 during NDP52-mediated mitophagy

TBK1 has been reported to play a role in PINK1/Parkin mitophagy,[37,41–45] but its role in mitophagy mediated individually by OPTN or NDP52 has not been explored. This is an important question because the two cargo receptors are not co-expressed in all cell types including neurons. In addition, given the finding that the ULK1/2 kinases are not essential for OPTN- or NDP52-mediated mitophagy (Figure 1), further investigation into TBK1 was warranted. First, we assessed the role of TBK1 kinase activity in recruiting the ULK1/2 complex by analyzing the mitochondrial recruitment of the ATG13 subunit. Upon mitophagy induction, inhibition of TBK1 kinase activity using BX795

Figure 2. FIP200 and ATG13 are essential for OPTN- and NDP52-mediated mitophagy

(A and B) penta KO, *ATG13* KO/penta KO, and *FIP200* KO/penta KO expressing BFP-Parkin and GFP-OPTN or GFP-NDP52 were treated with OA for 18 h and analyzed by immunoblotting (A) and COXII levels were quantified (B).

(C) Representative images of penta KO, and *FIP200* KO/penta KO expressing BFP-Parkin and GFP-OPTN or GFP-NDP52 immunostained for ATG13 and mitochondrial HSP60 after 1 h OA treatment. Untreated images shown in Figure S2C.

(D) Representative images of penta KO, and *ATG13* KO/penta KO expressing BFP-Parkin and GFP-OPTN or GFP-NDP52 immunostained for FIP200 and mitochondrial HSP60 after 1 h OA treatment. Untreated images shown in Figure S2D.

(E) Confocal images showing the recruitment of FIP200-GFP to glutathione sepharose beads coated with GST-tagged linear ubiquitin chain (GST-4xUb) and incubated with mCherry-NDP52. The cartoon insert depicts the experimental setup.

(F and G) Recruitment of mCherry-NDP52 to glutathione sepharose beads coated with GST-tagged linear ubiquitin chain (GST-4xUb) in the presence or absence of FIP200-GFP was analyzed by confocal imaging (F) and quantified (G). Data in (B) and (G) are mean ± SD from three independent experiments. ***$p < 0.001$, ****$p < 0.0001$ (one-way ANOVA; D); *$p \leq 0.05$ (Student's t test; I). Scale bars in (C) and (D): overviews, 10 μm; insets, 2 μm. Scale bars in (E) and (F) 100 μm.

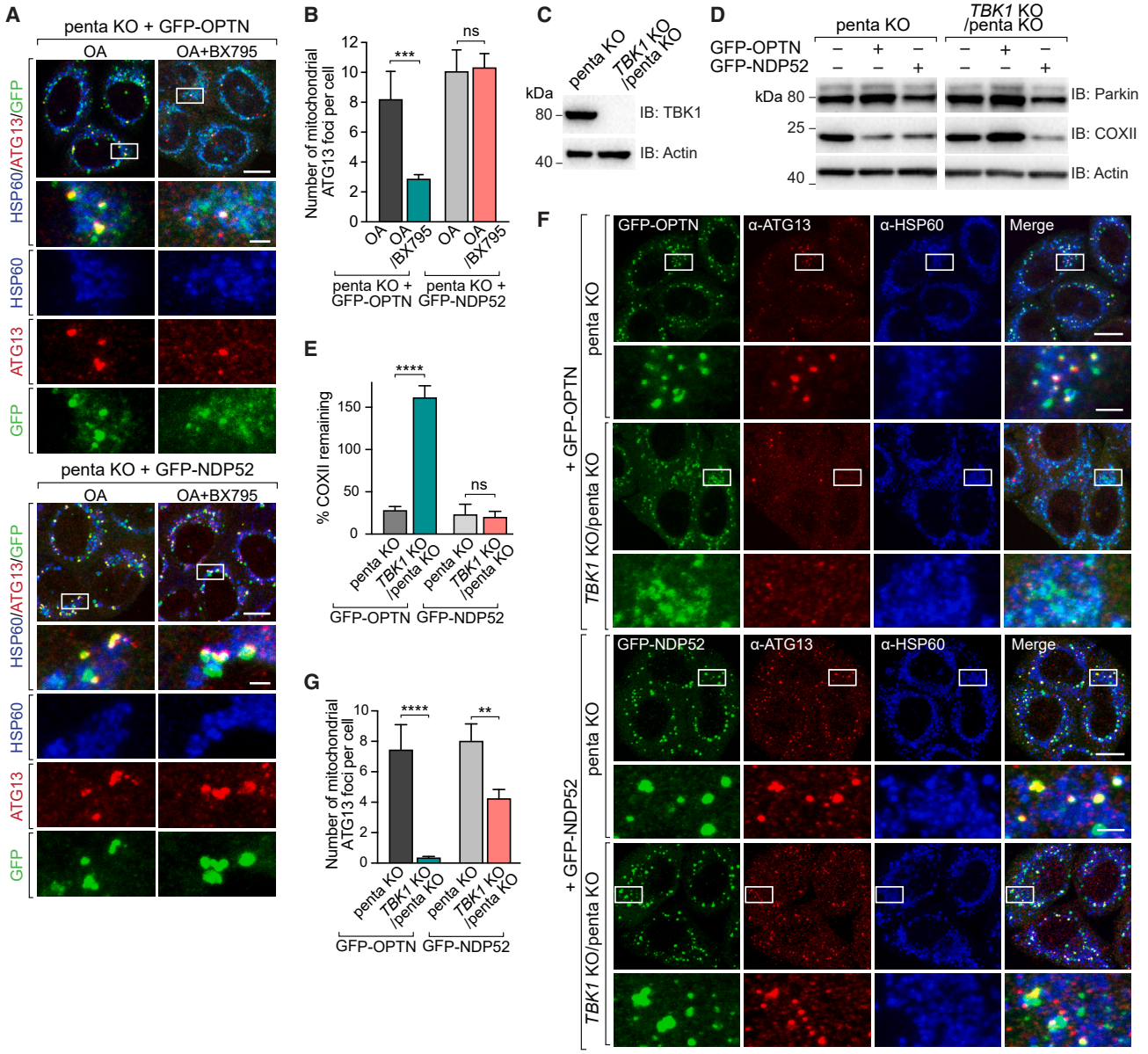

Figure 3. TBK1 is essential for OPTN-mediated mitophagy but not NDP52-mediated mitophagy

(A and B) penta KO cells expressing GFP-OPTN or GFP-NDP52 were treated with OA or OA and BX795 for 1 h and immunostained for ATG13 and mitochondrial HSP60 (A) and the number of mitochondrial ATG13 foci per cell was quantified (B).

(C) *TBK1* KO/penta KO was confirmed by immunoblotting (IB). kDa, kilodaltons.

(D and E) penta KO and *TBK1* KO/penta KO expressing BFP-Parkin and GFP-OPTN or GFP-NDP52 were treated with OA for 18 h and analyzed by immunoblotting (D) and COXII levels were quantified (E).

(F and G) penta KO and *TBK1* KO/penta KO expressing BFP-Parkin and GFP-OPTN or GFP-NDP52 treated with OA for 1 h and immunostained for ATG13 and mitochondrial HSP60 (F) and the number of mitochondrial ATG13 foci per cell was quantified (G). Untreated images shown in Figure S3A. Data in (B), (E), and (G) are mean ± SD from three independent experiments. *$p < 0.05$, **$p < 0.005$, ***$p < 0.001$, ****$p < 0.0001$ (one-way ANOVA). ns, not significant. Scale bars, overviews, 10 μm; insets, 2 μm.

significantly reduced mitochondrial recruitment of ATG13 in penta KO cells undergoing GFP-OPTN-mediated mitophagy, but not in cells utilizing GFP-NDP52 for mitophagy (Figures 3A and 3B). This result indicates that TBK1 kinase activity is required for the initiation of OPTN but not NDP52-mediated mitophagy. For further validation, and to address whether the kinase activity or the physical presence of TBK1 is necessary, TBK1 KOs were generated in the penta KO background (Figure 3C) and used to analyze mitophagy via COXII degradation and ULK1/2 complex recruitment via imaging of ATG13. In the absence of TBK1, GFP-OPTN failed to mediate COXII degradation (Figures 3D and 3E) and ATG13 recruitment to mitochondria

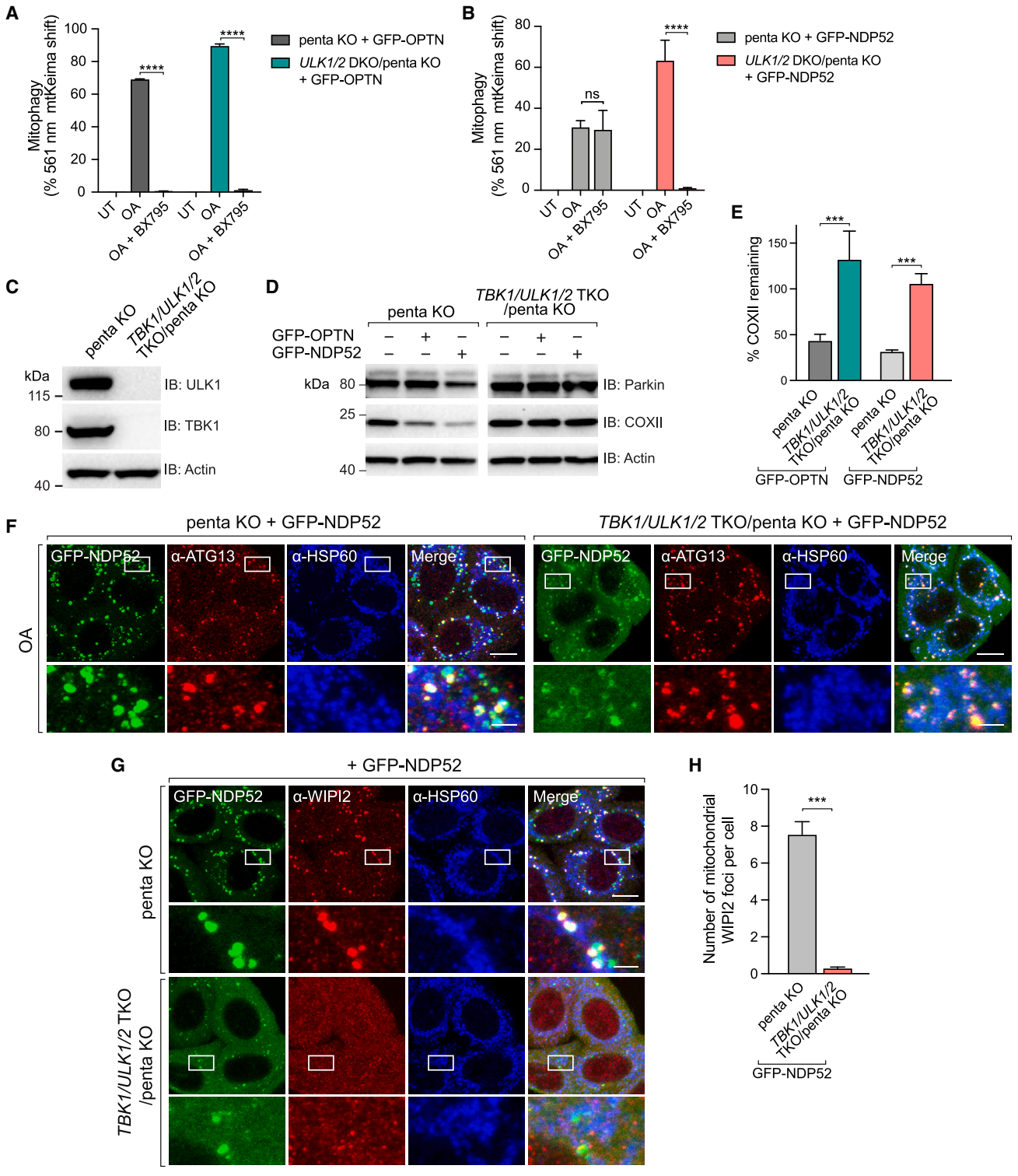

Figure 4. TBK1 and ULK1/2 function redundantly during NDP52-dependent mitophagy

(A and B) penta KO and *ULK1/2* DKO/penta KO cells expressing BFP-Parkin, mtKeima, and GFP-OPTN (A) or GFP-NDP52 (B) untreated or treated with OA or OA and BX795 for 4 h were analyzed by FACS. Lysosomal-positive mtKeima was calculated as the percentage of 561 nm mtKeima-positive cells. Representative FACS blots are provided in Figure S3B.

(C) *TBK1/ULK1/2* TKO/penta KO (TKO: triple knockout) was confirmed by immunoblotting (IB). kDa, kilodaltons.

(legend continued on next page)

(Figures 3F and 3G). By contrast, COXII degradation was unaffected by the loss of TBK1 during GFP-NDP52-dependent mitophagy (Figures 3D and 3E), although mitochondrial recruitment of ATG13 was significantly reduced (Figures 3F and 3G).

To confirm that the kinase activity of TBK1 is essential for OPTN-mediated mitophagy, *TBK1* KO/penta KO cells expressing GFP-OPTN were rescued with WT or D135N kinase dead (KD) TBK1. Mitophagy was assessed using the recently developed Halo mitophagy assay.[72] The Halo mitophagy assay measures mitophagy flux based on the generation of free Halo produced through lysosomal processing of a mitochondrially targeted Halo-GFP reporter construct (pSu9-Halo-mGFP).[72] $TBK1^{KD}$ did not rescue mitophagy (Figures S4A and S4B) nor mitochondrial ATG13 recruitment (Figure S4C), consistent with the results obtained with the TBK1 inhibitor BX795 (Figures 3A and 3B). We also investigated the role of OPTN-TBK1 binding during mitophagy using TBK1 mutants defective in OPTN binding. An E696K TBK1 mutant associated with ALS,[73–75] and a Δ667-729 C-terminal deletion (ΔCTD) mutant,[74] both defective in OPTN binding, were analyzed. The $TBK1^{E696K}$ and $TBK1^{\Delta CTD}$ mutants had greatly reduced interaction with TBK1 *in vitro* (Figures S4D and S4E), confirming previous observations.[73–75] In cells, the ability of $TBK1^{E696K}$ to bind OPTN was also disrupted (Figure S4F), along with significantly reduced mitophagy flux (Figures S4A and S4B), demonstrating that OPTN-TBK1 binding is important for OPTN-mediated mitophagy.[45,58] Taken together, these results demonstrate that TBK1 and its kinase activity are essential for the recruitment of the ULK1/2 complex and initiation of OPTN-mediated mitophagy. By contrast, TBK1 is largely dispensable for NDP52-mediated mitophagy, although it appears to regulate the efficiency of ULK1/2 complex recruitment and therefore mitophagy initiation by NDP52, as recently reported.[37]

Neither of the ULK1/2 or TBK1 kinases were essential for NDP52-mediated mitophagy (Figures 1, 2, and 3). However, given that some structural similarities between TBK1 and the ULK1/2 complex have been reported,[76] we asked whether TBK1 and ULK1/2 might function redundantly during NDP52-mediated mitophagy. Mitophagy rates using the mtKeima assay were analyzed in *ULK1/2* DKO/penta KO cells expressing either GFP-OPTN or GFP-NDP52 in the presence or absence of TBK1 inhibitor BX795. GFP-OPTN-mediated mitophagy was completely inhibited upon the addition of BX795 irrespective of the presence or absence of ULK1/2 (Figure 4A) supporting the absolute requirement of TBK1 kinase activity for OPTN-dependent mitophagy. By contrast, TBK1 kinase inhibition with BX795 was only able to prevent NDP52-dependent mitophagy when ULK1/2 were absent (Figure 4B). This demonstrates that TBK1 kinase activity compensates for the loss of ULK1/2 during NDP52-mediated mitophagy.

To further address the putative functional redundancy between TBK1 and ULK1/2 during NDP52-mediated mitophagy initiation and to ensure no off-target effects of BX795 on other kinases, TBK1 was knocked out in the *ULK1/2* DKO/penta KO background (Figure 4C). The combined deletion of TBK1 and ULK1/2 resulted in GFP-NDP52 losing its ability to drive COXII degradation (Figures 4D and 4E), demonstrating that ULK1/2 and TBK1 are functionally redundant in initiating NDP52-mediated mitophagy. Consistent with NDP52 being able to utilize TBK1, HA-NDP52 interacts with endogenous TBK1 in *ULK1/2* DKO/penta KO cells (Figure S5A). Given that NAP1 and SINTBAD can interact with both NDP52 and TBK1,[38,77–79] we asked if they mediate the interaction between NDP52 and TBK1. Using recombinant proteins combined with a fluorescence microscopy-based bead assay, GST-NDP52 attached to glutathione beads was only able to recruit TBK1 in the presence of NAP1 (Figures S5B and S5C) or SINTBAD (Figures S5D and S5E). This result demonstrates that NDP52 interacts with TBK1 via binding partners NAP1 or SINTBAD.

Next, we assessed where the mitophagy defect of NDP52 lies when ULK1/2 and TBK1 are absent. Analysis of ATG13 recruitment to mitochondria showed that consistent with its direct binding to FIP200, GFP-NDP52 was still able to support the recruitment of ATG13 in the absence of ULK1/2 and TBK1 (Figure 4F), demonstrating that a core complex consisting of FIP200, ATG13, and likely ATG101 remains intact.[76,80] However, the recruitment of WIPI2b, a PI(3)P effector protein, was completely abolished (Figures 4G and 4H), pointing toward a defect in the activation or recruitment of the PI3K complex. Our results therefore indicate that TBK1 is functionally redundant with ULK1/2 in promoting the activation of the PI3K complex, which is consistent with the role of ULK1/2 in enhancing the activity of the PI3K complex during starvation-induced autophagy.[64,66,81]

OPTN initiates mitophagy through an unconventional mechanism that is dependent on TBK1

A recent structural analysis revealed that peptides of OPTN and FIP200 interact *in vitro*,[59] indicating that OPTN follows the canonical mode of selective autophagy activation of directly recruiting the ULK1/2 complex via FIP200. However, our results show that OPTN is unable to stably recruit FIP200 in the absence of ATG13 (Figure 2D), arguing against FIP200 binding being the primary mitophagy initiation mechanism of OPTN. To directly address whether FIP200 binding, and therefore ULK1/2 complex recruitment, is the most upstream event of OPTN mitophagy initiation, we decided to block the next step of mitophagy involving PI3K complex recruitment. The rationale being that if the ULK1/2 complex is the most upstream event, then OPTN should retain the ability to recruit the ULK1/2 complex irrespective of downstream mitophagy steps. KO lines of ATG14, an essential and

(D and E) penta KO and *TBK1/ULK1/2* TKO/penta KO expressing BFP-Parkin and GFP-OPTN or GFP-NDP52 were treated with OA for 18 h and analyzed by immunoblotting (D) and COXII levels were quantified (E).

(F) penta KO and *TBK1/ULK1/2* TKO/penta KO cells expressing BFP-Parkin and GFP-NDP52 were immunostained for ATG13. (G and H) penta KO and *TBK1/ULK1/2* TKO/penta KO cells expressing BFP-Parkin and GFP-NDP52 were immunostained for WIPI2 and mitochondrial HSP60 (G) and the number of mitochondrial WIPI2 foci per cell was quantified (H). Representative images of untreated samples shown in Figures S3C and S3D. Data in (A), (B), (E), and (H) are mean ± SD from three independent experiments. *$p < 0.05$, **$p < 0.005$, ***$p < 0.001$, ****$p < 0.0001$ (A and B, two-way analysis of variance [ANOVA]; E and H one-way ANOVA). ns, not significant. Scale bars, overviews, 10 μm; insets, 2 μm.

specific subunit of the PI3K complex involved in autophagy, were generated in the penta KO background (Figure 5A). Analysis of COXII degradation confirmed that ATG14 is essential for PINK1/Parkin mitophagy mediated by either GFP-OPTN or GFP-NDP52 (Figures 5B and 5C). We also confirmed that the loss of ATG14 blocked activation of the PI3K complex as shown by the lack of mitochondrial recruitment of the PI(3)P effector protein WIPI2b (Figure 5F).

Next, mitochondrial recruitment of the ULK1/2 complex was analyzed by assessing ATG13 and FIP200 foci on mitochondria in the presence or absence of ATG14. During GFP-NDP52-mediated mitophagy, both ATG13 and FIP200 were recruited to damaged mitochondria irrespective of the presence or absence of ATG14 (Figures 5D, 5E, and S6B), aligning with NDP52's ability to directly bind and recruit FIP200 upstream of the PI3K complex.[37,38] However, by direct contrast, cells undergoing GFP-OPTN-mediated mitophagy failed to recruit ATG13 and FIP200 in cells lacking ATG14 (Figures 5D, 5E, and S6B), even though ULK1 kinase activity was unaffected (Figure S8D). ULK1 kinase activity was also unaffected by the loss of TBK1 (Figure S8D). These results argue for an unconventional mechanism of mitophagy activation by OPTN in which the PI3K complex is upstream of ULK1/2 complex recruitment but not required for ULK1 kinase activity (Figure S8D). Combined with the finding that TBK1 is essential for OPTN but not NDP52-mediated mitophagy, we conclude that mitophagy initiation by OPTN is mechanistically distinct from NDP52.

TBK1 directly binds to the PI3K complex

We next investigated whether OPTN can directly engage the PI3K complex by reconstituting mitophagy initiation *in vitro*. Ubiquitin-coated cargo mimetic beads were incubated with a TBK1 phospho-mimetic form of OPTN, termed OPTN S2D (S177D, S473D[82]), that was used to assess recruitment of the PI3K complex. Phosphomimetic OPTN S2D failed to recruit mCh-tagged PI3K complex (PI3Kc-mCh; mCh tag is on ATG14 subunit) to GST4xUb beads (Figure 6A), arguing against a direct binding model for OPTN mitophagy initiation. However, the PI3K complex was recruited upon the addition of GFP-TBK1 (Figure 6A). This led us to assess whether TBK1 can directly bind to the PI3K complex. Indeed, GFP-TBK1 alone tethered to GFP-Trap beads was sufficient to recruit the PI3K complex (Figure 6B). *In vitro* reconstitution of NDP52-mediated mitophagy initiation using ubiquitin-coated beads was conducted next. The analysis showed that NDP52 can directly recruit GFP-tagged ULK1 complex (ULK1c-GFP; Figure 6C), and this was sufficient to then recruit the PI3K complex (Figure 6D), indicating that purified ULK1 and PI3K complexes alone are sufficient for the two to directly interact. Another *in vitro* reconstitution in which the PI3K complex was immobilized onto RFP-Trap beads via mCh-ATG14 confirmed that a direct biochemical interaction exists between the ULK1 and PI3K complexes (Figure S7A).

Phospho-mass spectrometry analysis of purified PI3K complex was assessed using recombinant proteins incubated with recombinant TBK1 or ULK1 complex (Figure S8A). The analysis revealed that TBK1 and ULK1 phosphorylate all subunits of the PI3K complex, with most phosphorylation sites being shared between TBK1 and ULK1 (Figure S8A). The overlap of sites, and the fact that TBK1 can phosphorylate the PI3K complex, is consistent with the idea that TBK1 can function as an ULK1-like kinase during mitophagy. However, some specific TBK1 and ULK1 sites on the PI3K were also identified. For example, S29 and S383 on ATG14 were specific for ULK1, while phosphorylation of S227 on ATG14 and S165 on VPS34 were only detected in the presence of TBK1 (Figure S8A). Using a phospho-specific antibody for S29 on ATG14, we confirmed that phosphorylation of this site is mediated by ULK1 but not TBK1 *in vitro* (Figure S8B), and in cells (Figures S8C and S8D). S29 on ATG14 was shown to be important for PI3K complex activation during starvation autophagy.[81,83] However, given that phosphorylation of S29 on ATG14 was completely absent in *ULK1/2* DKO/penta KO (Figure S8C), and since *ULK1/2* DKO/penta KO expressing GFP-OPTN do not display a mitophagy defect (Figures 1B–1D), this site unlikely to be required for OPTN-mediated mitophagy, but we do not exclude a potential role for this site during NDP52-mediated mitophagy. Given that TBK1 can phosphorylate the PI3K complex similarly to ULK1, we conclude that TBK1 likely plays a role in PI3K complex activation, and therefore can function as a ULK1-like kinase during mitophagy. However, given that TBK1- and ULK1-specific sites were also identified, future work will need to be undertaken to clarify whether the precise activation mechanism is shared or distinct between TBK1 and ULK1.

The positioning of the PI3K complex upstream of ULK1/2 complex recruitment during OPTN-mediated mitophagy raised the question of how the ULK1/2 complex might be recruited by OPTN. Given that the PI3K and ULK1 complexes directly bind *in vitro* (Figure S7A) and have been reported to interact in cells,[83] it was decided to explore this area further. Using human cells, it has been proposed that the N-terminal HORMA (Hop1p, Rev1p and Mad2) domain within ATG13 interacts with ATG14,[83] whereas in yeast, it plays a role in the recruitment of ATG14.[84] We therefore assessed whether the HORMA domain of ATG13 is required for recruitment of the ULK1/2 complex during OPTN-mediated mitophagy. As can be seen in Figure 6E, deletion of the HORMA domain within ATG13 ($ATG13^{\Delta 1\text{-}198}$) prevented its recruitment to mitochondria during OPTN, but not NDP52, mediated mitophagy (Figure 6E). The ability of NDP52 to recruit $ATG13^{\Delta 1\text{-}198}$ is explained by NDP52's direct binding to FIP200 which interacts with the C terminus of ATG13.[76,80] Collectively, our results demonstrate that OPTN initiates autophagosome formation via direct interaction between TBK1 and the PI3K complex, whereas NDP52 initiates mitophagy via direct interaction with the ULK1/2 complex (Figure 7A), while the HORMA domain of ATG13 plays a linking role between the PI3K and ULK1/2 complexes. The linking role played by ATG13 explains how OPTN's unconventional mechanism of mitophagy initiation can proceed by first engaging with the PI3K complex through TBK1.

DISCUSSION

During PINK1/Parkin mitophagy, OPTN and NDP52 enable the recruitment of early autophagy machineries that initiate the *de*

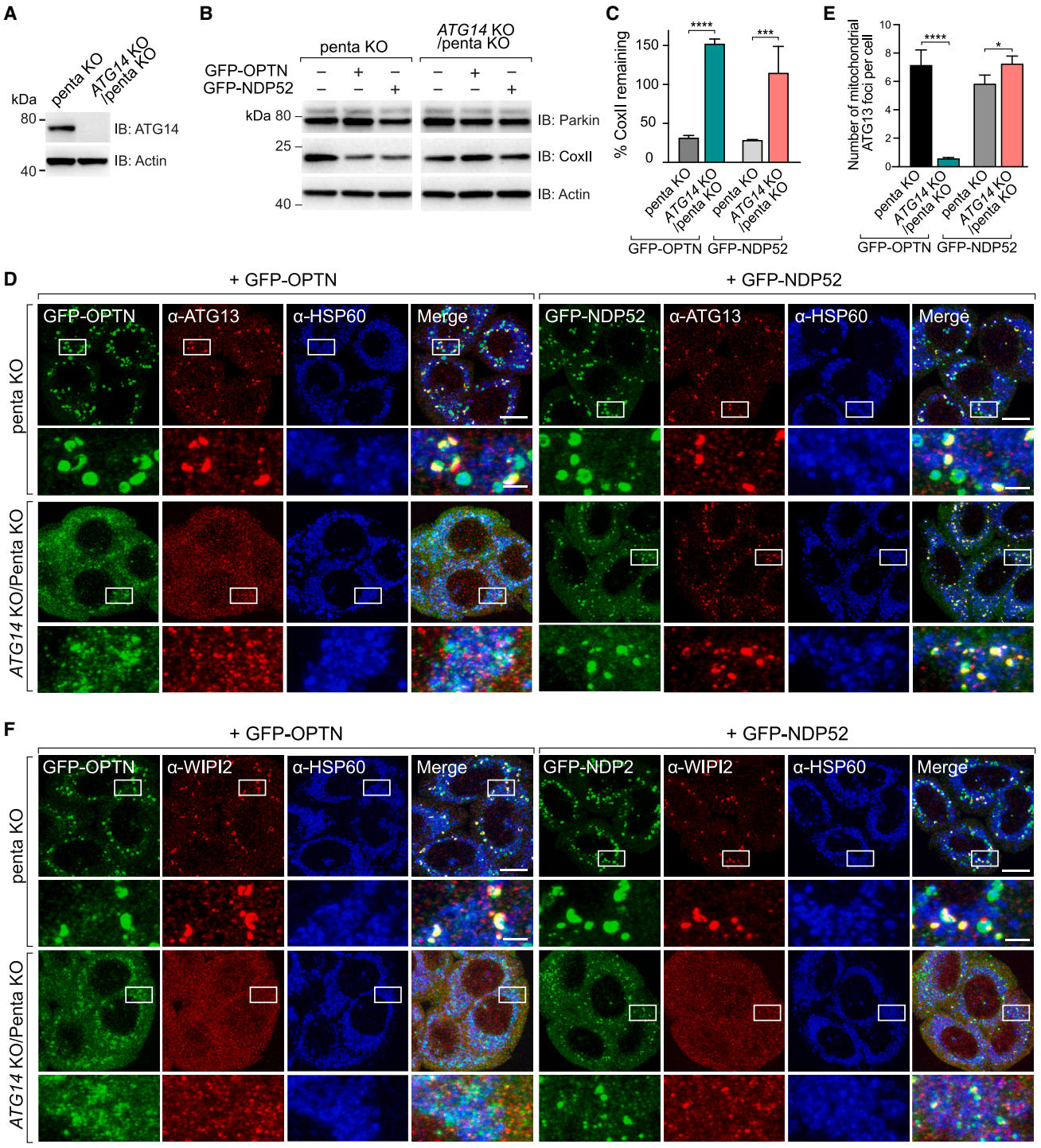

Figure 5. ATG14 is crucial for mitochondrial recruitment of the ATG13/FIP200 complex during OPTN-dependent mitophagy

(A) *ATG14* KO in penta KO background was confirmed by immunoblotting (IB). kDa, kilodaltons.

(B and C) penta KO and *ATG14* KO/penta KO expressing BFP-Parkin and GFP-OPTN or GFP-NDP52 were treated with OA for 18 h and analyzed by immunoblotting (B) and COXII levels were quantified (C).

(D–F) penta KO and *ATG14* KO/penta KO expressing BFP-Parkin and GFP-OPTN or GFP-NDP52 were treated with OA for 1 h and immunostained for ATG13 and mitochondrial HSP60 (D) or WIPI2 and mitochondrial HSP60 (F). The number of mitochondrial ATG13 foci per cell in (D) was also quantified (E). Representative images of untreated samples shown in Figures S6A and S6C. Data in (C) and (E) are mean ± SD from three independent experiments. *$p < 0.05$, **$p < 0.005$, ***$p < 0.001$, ****$p < 0.0001$ (one-way analysis of variance [ANOVA]). ns, not significant. Scale bars, overviews, 10 μm; insets, 2 μm.

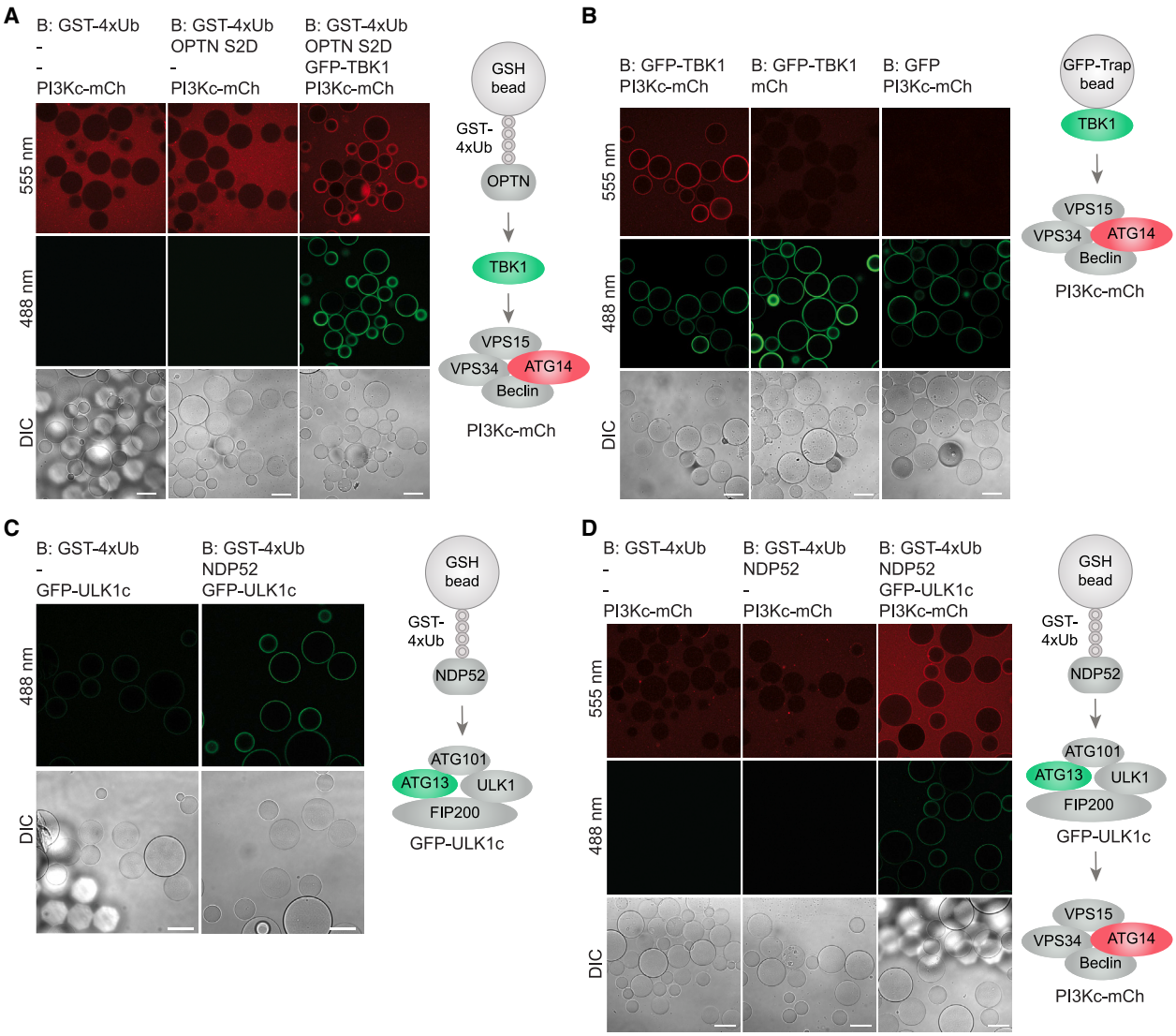

(legend on next page)

novo formation of autophagosomes on the surface of damaged mitochondria.[37,41] The mechanism of NDP52-mediated mitophagy initiation was recently revealed and involves NDP52 binding to the C-terminal part of FIP200 via an N-terminal SKICH domain.[37] The interaction between NDP52 and FIP200 enables recruitment and activation of the ULK1/2 complex through local clustering.[37] An analogous mechanism was identified during xenophagy for NDP52,[38] and for TAX1BP1 and p62 during aggrephagy.[39,40] The discovery that the LIR region of OPTN can also bind to the Claw domain of FIP200 *in vitro* indicated that OPTN also initiates selective autophagy in the same way. However, OPTN has also been reported to bind ATG9A in cells,[60] and to date, it has remained unclear exactly how OPTN initiates selective autophagy. The importance of understanding OPTN's initiation mechanism is highlighted by the fact that it is mutated in ALS,[62] is involved in PINK1/Parkin mitophagy linked to Parkinson's disease,[47,48,85] and is abundantly expressed in brain tissue where there is little to no NDP52.[41]

By delineating the initiation mechanism of OPTN in isolation during PINK1/Parkin mitophagy, we have revealed an unconventional pathway of selective autophagy initiation that is independent of FIP200 binding as the most upstream event. We propose a model in which OPTN's binding partner TBK1,[43,74] recruits/activates the PI3K complex via direct binding, which is linked to the ULK1/2 complex via the HORMA domain within ATG13 (Figures 6E and 7A), thereby bringing the ULK1/2 complex to the surface of mitochondria. Upon recruitment of the ULK1/2 complex, OPTN's interaction with FIP200[59] may become stabilized, and in combination with the recruitment of ATG9A vesicles via direct interaction with OPTN,[60] the formation of phagophore membranes is triggered (Figure 7B). The presence of ATG9A vesicles at this early stage likely provides lipids for generating the phagophore.[30–33,86] Whether the complex interplay of OPTN-mediated interactions is mutually exclusive to NDP52 mitophagy initiation remains to be determined. Although our data support that engagement of the PI3K complex occurs first via a direct interaction with TBK1, the recruitment of the PI3K and ULK1/2 complex to the autophagosome formation site is likely to be more complex and dynamic. Indeed, previous work has identified oscillatory recruitment of ATG13 and OPTN, as well as positive feedback loops between PI3K and ULK1/2 complex recruitment.[33,87] Whether TBK1-mediated phosphorylation of the PI3K and ULK1/2 complexes regulates the dynamics of initiation (Figure 7B), including OPTN binding to FIP200, warrants further investigation.

Given the essential role played by ULK1/2 kinases in starvation autophagy initiation,[80,88,89] it was reasonable to conclude that they should be essential for PINK1/Parkin mitophagy. Instead, we discovered that ULK1/2 are dispensable for mitophagy initiated by either OPTN or NDP52. More specifically, ULK1/2 are completely dispensable for OPTN-mediated mitophagy but are functionally redundant with TBK1 during NDP52-mediated mitophagy (Figure 4), although mitophagy through TBK1 appears to be slightly faster (Figure 1). A PINK1/Parkin independent form of mitophagy induced by ivermectin treatment also does not require ULK1/2 and is instead driven by TBK1,[87] while other autophagy pathways independent of ULK1/2 kinase activity have also been identified.[90–92] It is possible that TBK1 compensates for the loss of ULK1/2 in the ULK1/2 independent pathways. We propose that TBK1 can function as a selective autophagy-initiating kinase, akin to ULK1/2, but TBK1's role in selective autophagy will depend on which autophagy adaptor is involved. For example, TBK1 can play a dominant role during OPTN-mediated selective autophagy through stable direct binding.[43,74] Although the ULK1/2 kinases were not essential for PINK1/Parkin mitophagy (Figure 1), the ATG13 and FIP200 subunits were found to play an important role (Figure 2), highlighting the importance of key subunits of the ULK1/2 complex. During NDP52-mediated mitophagy, FIP200 was found to promote the recruitment of NDP52 both in cells and *in vitro* (Figure 2) in an apparent positive feedback loop. The discovery that membrane binding drives allosteric activation of ULK1/2 complex recruitment by FIP200 and NDP52 likely also contributes to the positive feedback loop in cells.[71]

In yeast, the HORMA domain of Atg13 was shown to be important for Atg14 recruitment to autophagosome formation sites during autophagy.[84] In mammalian systems, the PI3K complex has also been reported to interact with the ULK1 complex and this interaction is mediated by direct binding between ATG13 and ATG14 via the HORMA domain in ATG13.[83] OPTN and NDP52-mediated mitophagy is consistent with the HORMA domain of ATG13 playing a role in connecting the PI3K and ULK1/2 complexes (Figure 6), which is crucial for ULK1/2 complex recruitment during OPTN-mediated mitophagy. It would be interesting to investigate the role of the HORMA domain within ATG101, an ULK1/2 complex subunit that has been shown to dimerize with ATG13.[93,94] ATG101 could conceivably allow the simultaneous binding of the ULK1/2 complex to ATG9A and the PI3K complex to enhance autophagosome formation.[95]

Overall, our discovery that OPTN and NDP52 utilize distinct mechanisms to drive mitophagy initiation has broad implications for selective autophagy. It indicates that within the same type of selective autophagy, multiple mechanisms of initiation can be undertaken depending on which autophagy adaptors are present, and that can vary across different cell types and tissues. This finding can become important when it comes to targeting a particular selective autophagy pathway for therapeutic

Figure 6. PI3K complex directly interacts with TBK1 to allow mitochondrial recruitment of ATG13 during OPTN-mediated mitophagy

(A) Confocal images showing recruitment of GFP-TBK1 and PI3K complex-mCherry (PI3Kc-mCh) on cargo mimetic beads. Glutathione sepharose (GSH) beads were coated with GST-tagged linear ubiquitin chain (GST-4xUb) and incubated with indicated protein components and visualized by confocal microscope.
(B) Microscopy-based bead protein interaction assay with GFP-Trap beads using GFP or GFP-TBK1 as baits and mCherry (mCh) or PI3Kc-mCh as preys.
(C) Representative confocal images of GFP-ULK1 complex (GFP-ULK1c) recruitment to NDP52 bound to GST-tagged linear ubiquitin chain (GST-4xUb).
(D) Representative confocal images of PI3Kc-mCh recruitment to GST-4xUb/NDP52 axis via ULK1c-GFP. The cartoons in (A)–(D) depict the experimental setups.
(E) *ATG13* KO/penta KO cells expressing BFP-Parkin and GFP-OPTN or GFP-NDP52 rescued with HA-ATG13 or HA-ATG13$^{\Delta HORMA}$ were treated with OA for 1 h and immunostained for HA and mitochondrial HSP60. Untreated images shown in Figure S7B. Scale bars, (A–D) 100 μm; (D) overviews, 10 μm; insets, 2 μm.

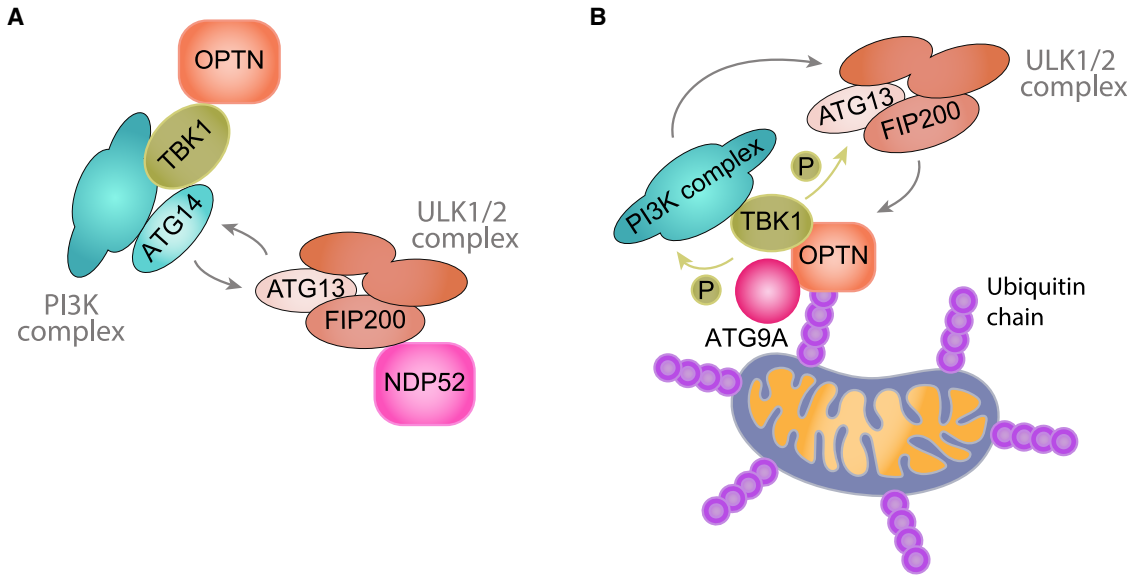

Figure 7. PI3K complex directly interacts with TBK1 to allow mitochondrial recruitment of ATG13 during OPTN-mediated mitophagy

(A) Schematic of the initiation complex bound to primary mitophagy adaptors OPTN and NDP52.

(B) A model for mitophagy initiation by OPTN. ATG9A-OPTN interaction and phosphorylation of the PI3K and ULK1/2 complex by TBK1 may contribute to the stabilization of the ULK1/2 complex on the mitochondrial surface.

purposes. For example, strategies to enhance PINK1/Parkin mitophagy in neurons that express high levels of OPTN will differ from that in tissues that express little to no OPTN, such as the heart and small intestine.[41] It would also be important to dissect whether the mechanism of mitophagy initiation driven by OPTN is more suited to the cell biology of a neuron. Digging deeper into the precise mechanisms of selective autophagy initiation mediated by each autophagy adaptor during different forms of selective autophagy is likely to yield therapeutic strategies to target damaged mitochondria, invading pathogens, and aggregating proteins in human disease.

Limitations of the study

Our study proposes that TBK1 functions as an ULK1/2-like kinase in the initiation of PINK1/Parkin mitophagy: during OPTN-mediated mitophagy, TBK1 directly binds to the PI3K complex to initiate autophagosome formation, analogous to how the ULK1/2 complex functions,[65,66,83,84] and during NDP52-mediated mitophagy, we find that TBK1 can function redundantly with ULK1/2. However, the molecular basis of TBK1's interaction with the PI3K complex, and the possible activation of its lipid kinase activity, remains to be determined. This includes which subunit/s of the complex TBK1 binds to and how this binding occurs. In addition, given that TBK1 can phosphorylate every subunit of the PI3K complex *in vitro* (Figure S8A), how these phosphorylation events might contribute to TBK1-PI3K interactions, and the activation of the PI3K complex, are important areas to address. Therefore, further investigation is required, including the identification of the critical TBK1-mediated phosphosites and the assessment of their role in PI3K activity. Given that many of the PI3K phosphosites are shared between TBK1 and ULK1/2, it is possible that their mechanism of PI3K activation may be as well. Analysis of the structural basis for TBK1-PI3K binding will also be necessary to fully tease apart how TBK1 initiates selective autophagy.

STAR★METHODS

Detailed methods are provided in the online version of this paper and include the following:

- KEY RESOURCES TABLE
- RESOURCE AVAILABILITY
  - Lead contact
  - Materials availability
  - Data and code availability
- EXPERIMENTAL MODEL AND SUBJECT DETAILS
- METHOD DETAILS
  - Antibodies and reagents
  - Generation of knockout lines using CRISPR/Cas9 gene editing
  - Cloning and generation of stable cell lines
  - Mitophagy treatment and immunoblotting
  - Immunoprecipitation with anti-HA magnetic beads
- IMMUNOFLUORESCENCE ASSAY AND CONFOCAL IMAGE ANALYSIS
  - Mito-Keima autophagosome-lysosome fusion mitophagy assay
  - Halo assay to assess mitophagy flux
  - Transmission electron microscopy imaging
  - Protein expressions and purification
  - Microscopy-based bead protein-protein interaction assay
  - *In vitro* kinase assay

- Mass spectrometry analysis, data analysis and figure preparation
- QUANTIFICATION AND STATISTICAL ANALYSIS

SUPPLEMENTAL INFORMATION

Supplemental information can be found online at https://doi.org/10.1016/j.molcel.2023.04.021.

ACKNOWLEDGMENTS

We thank members of the Larazou Lab and others in Aligning Science Across Parkinson's (ASAP) Team mito911 for their advice and discussions. We thank the laboratory of Noboru Mizushima (The University of Tokyo) for sharing *FIP200* KO/penta KO cells and the laboratory of Mike Ryan (Monash Biomedicine Discovery Institute, Monash University) for sharing anti-B17.2L antibodies. We also thank the Monash Flow Cytometry Platform (FlowCore), the Monash Micro Imaging Platform, the Ramaciotti Centre for Cryo-Electron Microscopy, and the Max Perutz Labs BioOptics and Mass Spectrometry facilities for their technical support.

This work was supported by the National Health and Medical Research Council (NHMRC) (GNT1106471 to M.L.), the Australian Research Council (ARC) Discovery Project (DP200100347 to M.L.), the Human Frontiers Science Program RGP0026/2017 (to S.M.), a research and travel grant from the Flanders Fund for Scientific Research (FWO-Flanders to E.A.), and a Marie Skłodowska-Curie MSCA Postdoctoral Fellowship (101062916 to E.A.). This research was also funded in whole or in part by Aligning Science Across Parkinson's (ASAP-000350 to S.M. and M.L.) through the Michael J. Fox Foundation for Parkinson's Research (MJFF). For the purpose of open access, the author has applied a CC BY public copyright license to all author-accepted manuscripts arising from this submission.

AUTHOR CONTRIBUTIONS

T.N.N. and M.L. conceived the projects. T.N.N., J.S.-M., S.M., and M.L. designed the experiments. T.N.N., J.S.-M., G.K., W.K.L., E.A., D.F., S.S., D.B., B.S.P., M.S., and R.S.J.L. performed the experiments. T.N.N. and M.L. wrote the manuscript, and all authors contributed to preparing and editing the manuscript.

DECLARATION OF INTERESTS

S.M. is a member of the scientific advisory board of Casma Therapeutics. M.L. is a member of the scientific advisory board and co-founder of Automera.

INCLUSION AND DIVERSITY

We support inclusive, diverse, and equitable conduct of research.

Received: September 16, 2022
Revised: March 6, 2023
Accepted: April 19, 2023
Published: May 18, 2023

REFERENCES

1. Dikic, I., and Elazar, Z. (2018). Mechanism and medical implications of mammalian autophagy. Nat. Rev. Mol. Cell Biol. *19*, 349–364. https://doi.org/10.1038/s41580-018-0003-4.
2. Melia, T.J., Lystad, A.H., and Simonsen, A. (2020). Autophagosome biogenesis: from membrane growth to closure. J. Cell Biol. *219*. https://doi.org/10.1083/jcb.202002085.
3. Axe, E.L., Walker, S.A., Manifava, M., Chandra, P., Roderick, H.L., Habermann, A., Griffiths, G., and Ktistakis, N.T. (2008). Autophagosome formation from membrane compartments enriched in phosphatidylinositol 3-phosphate and dynamically connected to the endoplasmic reticulum. J. Cell Biol. *182*, 685–701. https://doi.org/10.1083/jcb.200803137.
4. Hayashi-Nishino, M., Fujita, N., Noda, T., Yamaguchi, A., Yoshimori, T., and Yamamoto, A. (2009). A subdomain of the endoplasmic reticulum forms a cradle for autophagosome formation. Nat. Cell Biol. *11*, 1433–1437. https://doi.org/10.1038/ncb1991.
5. Uemura, T., Yamamoto, M., Kametaka, A., Sou, Y.S., Yabashi, A., Yamada, A., Annoh, H., Kametaka, S., Komatsu, M., and Waguri, S. (2014). A cluster of thin tubular structures mediates transformation of the endoplasmic reticulum to autophagic isolation membrane. Mol. Cell. Biol. *34*, 1695–1706. https://doi.org/10.1128/MCB.01327-13.
6. Kishi-Itakura, C., Koyama-Honda, I., Itakura, E., and Mizushima, N. (2014). Ultrastructural analysis of autophagosome organization using mammalian autophagy-deficient cells. J. Cell Sci. *127*, 4089–4102. https://doi.org/10.1242/jcs.156034.
7. Itakura, E., and Mizushima, N. (2010). Characterization of autophagosome formation site by a hierarchical analysis of mammalian Atg proteins. Autophagy *6*, 764–776. https://doi.org/10.4161/auto.6.6.12709.
8. Yang, Z., and Klionsky, D.J. (2010). Eaten alive: a history of macroautophagy. Nat. Cell Biol. *12*, 814–822. https://doi.org/10.1038/ncb0910-814.
9. Mizushima, N., Yoshimori, T., and Ohsumi, Y. (2011). The role of Atg proteins in autophagosome formation. Annu. Rev. Cell Dev. Biol. *27*, 107–132. https://doi.org/10.1146/annurev-cellbio-092910-154005.
10. Dooley, H.C., Razi, M., Polson, H.E., Girardin, S.E., Wilson, M.I., and Tooze, S.A. (2014). WIPI2 links LC3 conjugation with PI3P, autophagosome formation, and pathogen clearance by recruiting Atg12-5-16L1. Mol. Cell *55*, 238–252. https://doi.org/10.1016/j.molcel.2014.05.021.
11. Ichimura, Y., Kirisako, T., Takao, T., Satomi, Y., Shimonishi, Y., Ishihara, N., Mizushima, N., Tanida, I., Kominami, E., Ohsumi, M., et al. (2000). A ubiquitin-like system mediates protein lipidation. Nature *408*, 488–492. https://doi.org/10.1038/35044114.
12. Mizushima, N., Noda, T., Yoshimori, T., Tanaka, Y., Ishii, T., George, M.D., Klionsky, D.J., Ohsumi, M., and Ohsumi, Y. (1998). A protein conjugation system essential for autophagy. Nature *395*, 395–398. https://doi.org/10.1038/26506.
13. Deretic, V., and Lazarou, M. (2022). A guide to membrane atg8ylation and autophagy with reflections on immunity. J. Cell Biol. *221*. https://doi.org/10.1083/jcb.202203083.
14. Kumar, S., Jia, J.Y., and Deretic, V. (2021). Atg8ylation as a general membrane stress and remodeling response. Cell Stress *5*, 128–142. https://doi.org/10.15698/cst2021.09.255.
15. Nguyen, T.N., Padman, B.S., Zellner, S., Khuu, G., Uoselis, L., Lam, W.K., Skulsuppaisarn, M., Lindblom, R.S.J., Watts, E.M., Behrends, C., et al. (2021). ATG4 family proteins drive phagophore growth independently of the LC3/GABARAP lipidation system. Mol. Cell *81,* 2013–2030.e9. https://doi.org/10.1016/j.molcel.2021.03.001.
16. Agrotis, A., von Chamier, L., Oliver, H., Kiso, K., Singh, T., and Ketteler, R. (2019). Human ATG4 autophagy proteases counteract attachment of ubiquitin-like LC3/GABARAP proteins to other cellular proteins. J. Biol. Chem. *294*, 12610–12621. https://doi.org/10.1074/jbc.AC119.009977.
17. Nakatogawa, H., Ichimura, Y., and Ohsumi, Y. (2007). Atg8, a ubiquitin-like protein required for autophagosome formation, mediates membrane tethering and hemifusion. Cell *130*, 165–178. https://doi.org/10.1016/j.cell.2007.05.021.
18. Martens, S., and Fracchiolla, D. (2020). Activation and targeting of ATG8 protein lipidation. Cell Discov. *6*, 23. https://doi.org/10.1038/s41421-020-0155-1.
19. Lamark, T., and Johansen, T. (2021). Mechanisms of selective autophagy. Annu. Rev. Cell Dev. Biol. *37*, 143–169. https://doi.org/10.1146/annurev-cellbio-120219-035530.
20. Chowdhury, S., Otomo, C., Leitner, A., Ohashi, K., Aebersold, R., Lander, G.C., and Otomo, T. (2018). Insights into autophagosome biogenesis from structural and biochemical analyses of the ATG2A-WIPI4 complex.

Proc. Natl. Acad. Sci. USA *115,* E9792–E9801. https://doi.org/10.1073/pnas.1811874115.

21. Kotani, T., Kirisako, H., Koizumi, M., Ohsumi, Y., and Nakatogawa, H. (2018). The Atg2-Atg18 complex tethers pre-autophagosomal membranes to the endoplasmic reticulum for autophagosome formation. Proc. Natl. Acad. Sci. USA *115*, 10363–10368. https://doi.org/10.1073/pnas.1806727115.
22. Maeda, S., Otomo, C., and Otomo, T. (2019). The autophagic membrane tether ATG2A transfers lipids between membranes. eLife *8,* e45777. https://doi.org/10.7554/eLife.45777.
23. Osawa, T., Kotani, T., Kawaoka, T., Hirata, E., Suzuki, K., Nakatogawa, H., Ohsumi, Y., and Noda, N.N. (2019). Atg2 mediates direct lipid transfer between membranes for autophagosome formation. Nat. Struct. Mol. Biol. *26*, 281–288. https://doi.org/10.1038/s41594-019-0203-4.
24. Valverde, D.P., Yu, S.L., Boggavarapu, V., Kumar, N., Lees, J.A., Walz, T., Reinisch, K.M., and Melia, T.J. (2019). ATG2 transports lipids to promote autophagosome biogenesis. J. Cell Biol. *218*, 1787–1798. https://doi.org/10.1083/jcb.201811139.
25. Zheng, J.X., Li, Y., Ding, Y.H., Liu, J.J., Zhang, M.J., Dong, M.Q., Wang, H.W., and Yu, L. (2017). Architecture of the ATG2B-WDR45 complex and an aromatic Y/HF motif crucial for complex formation. Autophagy *13*, 1870–1883. https://doi.org/10.1080/15548627.2017.1359381.
26. Ghanbarpour, A., Valverde, D.P., Melia, T.J., and Reinisch, K.M. (2021). A model for a partnership of lipid transfer proteins and scramblases in membrane expansion and organelle biogenesis. Proc. Natl. Acad. Sci. USA *118*. https://doi.org/10.1073/pnas.2101562118.
27. Maeda, S., Yamamoto, H., Kinch, L.N., Garza, C.M., Takahashi, S., Otomo, C., Grishin, N.V., Forli, S., Mizushima, N., and Otomo, T. (2020). Structure, lipid scrambling activity and role in autophagosome formation of ATG9A. Nat. Struct. Mol. Biol. *27*, 1194–1201. https://doi.org/10.1038/s41594-020-00520-2.
28. Matoba, K., Kotani, T., Tsutsumi, A., Tsuji, T., Mori, T., Noshiro, D., Sugita, Y., Nomura, N., Iwata, S., Ohsumi, Y., et al. (2020). Atg9 is a lipid scramblase that mediates autophagosomal membrane expansion. Nat. Struct. Mol. Biol. *27*, 1185–1193. https://doi.org/10.1038/s41594-020-00518-w.
29. Gómez-Sánchez, R., Rose, J., Guimarães, R., Mari, M., Papinski, D., Rieter, E., Geerts, W.J., Hardenberg, R., Kraft, C., Ungermann, C., et al. (2018). Atg9 establishes Atg2-dependent contact sites between the endoplasmic reticulum and phagophores. J. Cell Biol. *217*, 2743–2763. https://doi.org/10.1083/jcb.201710116.
30. Judith, D., Jefferies, H.B.J., Boeing, S., Frith, D., Snijders, A.P., and Tooze, S.A. (2019). ATG9A shapes the forming autophagosome through Arfaptin 2 and phosphatidylinositol 4-kinase III beta. J. Cell Biol. *218*, 1634–1652. https://doi.org/10.1083/jcb.201901115.
31. Sawa-Makarska, J., Baumann, V., Coudevylle, N., von Bülow, S., Nogellova, V., Abert, C., Schuschnig, M., Graef, M., Hummer, G., and Martens, S. (2020). Reconstitution of autophagosome nucleation defines Atg9 vesicles as seeds for membrane formation. Science *369,* eaaz7714. https://doi.org/10.1126/science.aaz7714.
32. Mari, M., Griffith, J., Rieter, E., Krishnappa, L., Klionsky, D.J., and Reggiori, F. (2010). An Atg9-containing compartment that functions in the early steps of autophagosome biogenesis. J. Cell Biol. *190*, 1005–1022. https://doi.org/10.1083/jcb.200912089.
33. Karanasios, E., Stapleton, E., Manifava, M., Kaizuka, T., Mizushima, N., Walker, S.A., and Ktistakis, N.T. (2013). Dynamic association of the ULK1 complex with omegasomes during autophagy induction. J. Cell Sci. *126*, 5224–5238. https://doi.org/10.1242/jcs.132415.
34. Mizushima, N. (2020). The ATG conjugation systems in autophagy. Curr. Opin. Cell Biol. *63*, 1–10. https://doi.org/10.1016/j.ceb.2019.12.001.
35. Gatica, D., Lahiri, V., and Klionsky, D.J. (2018). Cargo recognition and degradation by selective autophagy. Nat. Cell Biol. *20*, 233–242. https://doi.org/10.1038/s41556-018-0037-z.
36. Goodall, E.A., Kraus, F., and Harper, J.W. (2022). Mechanisms underlying ubiquitin-driven selective mitochondrial and bacterial autophagy. Mol. Cell *82*, 1501–1513. https://doi.org/10.1016/j.molcel.2022.03.012.
37. Vargas, J.N.S., Wang, C., Bunker, E., Hao, L., Maric, D., Schiavo, G., Randow, F., and Youle, R.J. (2019). Spatiotemporal control of ULK1 activation by NDP52 and TBK1 during selective autophagy. Mol. Cell *74,* 347–362.e6. https://doi.org/10.1016/j.molcel.2019.02.010.
38. Ravenhill, B.J., Boyle, K.B., von Muhlinen, N., Ellison, C.J., Masson, G.R., Otten, E.G., Foeglein, A., Williams, R., and Randow, F. (2019). The cargo receptor NDP52 initiates selective autophagy by recruiting the ULK complex to cytosol-invading bacteria. Mol. Cell *74,* 320–329.e6. https://doi.org/10.1016/j.molcel.2019.01.041.
39. Turco, E., Savova, A., Gere, F., Ferrari, L., Romanov, J., Schuschnig, M., and Martens, S. (2021). Reconstitution defines the roles of p62, NBR1 and TAX1BP1 in ubiquitin condensate formation and autophagy initiation. Nat. Commun. *12*, 5212. https://doi.org/10.1038/s41467-021-25572-w.
40. Turco, E., Witt, M., Abert, C., Bock-Bierbaum, T., Su, M.Y., Trapannone, R., Sztacho, M., Danieli, A., Shi, X.S., Zaffagnini, G., et al. (2019). FIP200 claw domain binding to p62 promotes autophagosome formation at ubiquitin condensates. Mol. Cell *74,* 330–346.e11. https://doi.org/10.1016/j.molcel.2019.01.035.
41. Lazarou, M., Sliter, D.A., Kane, L.A., Sarraf, S.A., Wang, C., Burman, J.L., Sideris, D.P., Fogel, A.I., and Youle, R.J. (2015). The ubiquitin kinase PINK1 recruits autophagy receptors to induce mitophagy. Nature *524*, 309–314. https://doi.org/10.1038/nature14893.
42. Heo, J.M., Ordureau, A., Paulo, J.A., Rinehart, J., and Harper, J.W. (2015). The PINK1-Parkin mitochondrial ubiquitylation pathway drives a program of OPTN/NDP52 recruitment and TBK1 activation to promote mitophagy. Mol. Cell *60*, 7–20. https://doi.org/10.1016/j.molcel.2015.08.016.
43. Richter, B., Sliter, D.A., Herhaus, L., Stolz, A., Wang, C., Beli, P., Zaffagnini, G., Wild, P., Martens, S., Wagner, S.A., et al. (2016). Phosphorylation of OPTN by TBK1 enhances its binding to Ub chains and promotes selective autophagy of damaged mitochondria. Proc. Natl. Acad. Sci. USA *113*, 4039–4044. https://doi.org/10.1073/pnas.1523926113.
44. Heo, J.M., Ordureau, A., Swarup, S., Paulo, J.A., Shen, K., Sabatini, D.M., and Harper, J.W. (2018). RAB7A phosphorylation by TBK1 promotes mitophagy via the PINK-Parkin pathway. Sci. Adv. *4,* eaav0443. https://doi.org/10.1126/sciadv.aav0443.
45. Moore, A.S., and Holzbaur, E.L. (2016). Dynamic recruitment and activation of ALS-associated TBK1 with its target optineurin are required for efficient mitophagy. Proc. Natl. Acad. Sci. USA *113,* E3349–E3358. https://doi.org/10.1073/pnas.1523810113.
46. Mizushima, N., and Levine, B. (2020). Autophagy in human diseases. N. Engl. J. Med. *383*, 1564–1576. https://doi.org/10.1056/NEJMra2022774.
47. Kitada, T., Asakawa, S., Hattori, N., Matsumine, H., Yamamura, Y., Minoshima, S., Yokochi, M., Mizuno, Y., and Shimizu, N. (1998). Mutations in the parkin gene cause autosomal recessive juvenile parkinsonism. Nature *392*, 605–608. https://doi.org/10.1038/33416.
48. Valente, E.M., Abou-Sleiman, P.M., Caputo, V., Muqit, M.M.K., Harvey, K., Gispert, S., Ali, Z., Del Turco, D., Bentivoglio, A.R., Healy, D.G., et al. (2004). Hereditary early-onset Parkinson's disease caused by mutations in PINK1. Science *304*, 1158–1160. https://doi.org/10.1126/science.1096284.
49. Narendra, D., Tanaka, A., Suen, D.F., and Youle, R.J. (2008). Parkin is recruited selectively to impaired mitochondria and promotes their autophagy. J. Cell Biol. *183*, 795–803. https://doi.org/10.1083/jcb.200809125.
50. Narendra, D.P., Jin, S.M., Tanaka, A., Suen, D.F., Gautier, C.A., Shen, J., Cookson, M.R., and Youle, R.J. (2010). PINK1 is selectively stabilized on impaired mitochondria to activate parkin. PLoS Biol. *8,* e1000298. https://doi.org/10.1371/journal.pbio.1000298.

51. Kane, L.A., Lazarou, M., Fogel, A.I., Li, Y., Yamano, K., Sarraf, S.A., Banerjee, S., and Youle, R.J. (2014). PINK1 phosphorylates ubiquitin to activate Parkin E3 ubiquitin ligase activity. J. Cell Biol. *205*, 143–153. https://doi.org/10.1083/jcb.201402104.

52. Koyano, F., Okatsu, K., Kosako, H., Tamura, Y., Go, E., Kimura, M., Kimura, Y., Tsuchiya, H., Yoshihara, H., Hirokawa, T., et al. (2014). Ubiquitin is phosphorylated by PINK1 to activate parkin. Nature *510*, 162–166. https://doi.org/10.1038/nature13392.

53. Ordureau, A., Sarraf, S.A., Duda, D.M., Heo, J.M., Jedrychowski, M.P., Sviderskiy, V.O., Olszewski, J.L., Koerber, J.T., Xie, T., Beausoleil, S.A., et al. (2014). Quantitative proteomics reveal a feedforward mechanism for mitochondrial Parkin translocation and ubiquitin chain synthesis. Mol. Cell *56*, 360–375. https://doi.org/10.1016/j.molcel.2014.09.007.

54. Wauer, T., Simicek, M., Schubert, A., and Komander, D. (2015). Mechanism of phospho-ubiquitin-induced Parkin activation. Nature *524*, 370–374. https://doi.org/10.1038/nature14879.

55. Wong, Y.C., and Holzbaur, E.L. (2014). Optineurin is an autophagy receptor for damaged mitochondria in parkin-mediated mitophagy that is disrupted by an ALS-linked mutation. Proc. Natl. Acad. Sci. USA *111,* E4439–E4448. https://doi.org/10.1073/pnas.1405752111.

56. Padman, B.S., Nguyen, T.N., Uoselis, L., Skulsuppaisarn, M., Nguyen, L.K., and Lazarou, M. (2019). LC3/GABARAPs drive ubiquitin-independent recruitment of optineurin and NDP52 to amplify mitophagy. Nat. Commun. *10*, 408. https://doi.org/10.1038/s41467-019-08335-6.

57. Wild, P., Farhan, H., McEwan, D.G., Wagner, S., Rogov, V.V., Brady, N.R., Richter, B., Korac, J., Waidmann, O., Choudhary, C., et al. (2011). Phosphorylation of the autophagy receptor optineurin restricts Salmonella growth. Science *333*, 228–233. https://doi.org/10.1126/science.1205405.

58. Yamano, K., Sawada, M., Kikuchi, R., Nagataki, K., Kojima, W., Sugihara, A., Fujino, T., Tanaka, K., Hayashi, G., Murakami, H., et al. (2023). Optineurin provides a mitophagy contact site for TBK1 activation. Preprint at bioRxiv. https://doi.org/10.1101/2023.02.24.529790.

59. Zhou, Z., Liu, J., Fu, T., Wu, P., Peng, C., Gong, X., Wang, Y., Zhang, M., Li, Y., Wang, Y., et al. (2021). Phosphorylation regulates the binding of autophagy receptors to FIP200 Claw domain for selective autophagy initiation. Nat. Commun. *12*, 1570. https://doi.org/10.1038/s41467-021-21874-1.

60. Yamano, K., Kikuchi, R., Kojima, W., Hayashida, R., Koyano, F., Kawawaki, J., Shoda, T., Demizu, Y., Naito, M., Tanaka, K., et al. (2020). Critical role of mitochondrial ubiquitination and the OPTN-ATG9A axis in mitophagy. J. Cell Biol. *219*. https://doi.org/10.1083/jcb.201912144.

61. Gómez-Sánchez, R., Tooze, S.A., and Reggiori, F. (2021). Membrane supply and remodeling during autophagosome biogenesis. Curr. Opin. Cell Biol. *71*, 112–119. https://doi.org/10.1016/j.ceb.2021.02.001.

62. Maruyama, H., Morino, H., Ito, H., Izumi, Y., Kato, H., Watanabe, Y., Kinoshita, Y., Kamada, M., Nodera, H., Suzuki, H., et al. (2010). Mutations of optineurin in amyotrophic lateral sclerosis. Nature *465*, 223–226. https://doi.org/10.1038/nature08971.

63. Rezaie, T., Child, A., Hitchings, R., Brice, G., Miller, L., Coca-Prados, M., Héon, E., Krupin, T., Ritch, R., Kreutzer, D., et al. (2002). Adult-onset primary open-angle glaucoma caused by mutations in optineurin. Science *295*, 1077–1079. https://doi.org/10.1126/science.1066901.

64. Mercer, T.J., Gubas, A., and Tooze, S.A. (2018). A molecular perspective of mammalian autophagosome biogenesis. J. Biol. Chem. *293*, 5386–5395. https://doi.org/10.1074/jbc.R117.810366.

65. Egan, D.F., Chun, M.G., Vamos, M., Zou, H., Rong, J., Miller, C.J., Lou, H.J., Raveendra-Panickar, D., Yang, C.C., Sheffler, D.J., et al. (2015). Small molecule inhibition of the autophagy kinase ULK1 and identification of ULK1 substrates. Mol. Cell *59*, 285–297. https://doi.org/10.1016/j.molcel.2015.05.031.

66. Mercer, T.J., Ohashi, Y., Boeing, S., Jefferies, H.B.J., De Tito, S., Flynn, H., Tremel, S., Zhang, W., Wirth, M., Frith, D., et al. (2021). Phosphoproteomic identification of ULK substrates reveals VPS15-dependent ULK/VPS34 interplay in the regulation of autophagy. EMBO J. *40*. e105985. https://doi.org/10.15252/embj.2020105985.

67. Katayama, H., Kogure, T., Mizushima, N., Yoshimori, T., and Miyawaki, A. (2011). A sensitive and quantitative technique for detecting autophagic events based on lysosomal delivery. Chem. Biol. *18*, 1042–1052. https://doi.org/10.1016/j.chembiol.2011.05.013.

68. Hara, T., Takamura, A., Kishi, C., Iemura, S.I., Natsume, T., Guan, J.L., and Mizushima, N. (2008). FIP200, a ULK-interacting protein, is required for autophagosome formation in mammalian cells. J. Cell Biol. *181*, 497–510. https://doi.org/10.1083/jcb.200712064.

69. Kaizuka, T., and Mizushima, N. (2016). Atg13 is essential for autophagy and cardiac development in mice. Mol. Cell. Biol. *36*, 585–595. https://doi.org/10.1128/MCB.01005-15.

70. Abert, C., and Martens, S. (2019). Studies of receptor-Atg8 interactions during selective autophagy. Methods Mol. Biol. *1880*, 189–196. https://doi.org/10.1007/978-1-4939-8873-0_11.

71. Shi, X., Chang, C., Yokom, A.L., Jensen, L.E., and Hurley, J.H. (2020). The autophagy adaptor NDP52 and the FIP200 coiled-coil allosterically activate ULK1 complex membrane recruitment. eLife *9*. https://doi.org/10.7554/eLife.59099.

72. Yim, W.W., Yamamoto, H., and Mizushima, N. (2022). A pulse-chasable reporter processing assay for mammalian autophagic flux with HaloTag. eLife *11*. https://doi.org/10.7554/eLife.78923.

73. Freischmidt, A., Wieland, T., Richter, B., Ruf, W., Schaeffer, V., Müller, K., Marroquin, N., Nordin, F., Hübers, A., Weydt, P., et al. (2015). Haploinsufficiency of TBK1 causes familial ALS and fronto-temporal dementia. Nat. Neurosci. *18*, 631–636. https://doi.org/10.1038/nn.4000.

74. Li, F.X., Xie, X.Q., Wang, Y.L., Liu, J.P., Cheng, X.F., Guo, Y.J., Gong, Y.K., Hu, S.C., and Pan, L.F. (2016). Structural insights into the interaction and disease mechanism of neurodegenerative disease-associated optineurin and TBK1 proteins. Nat. Commun. *7*, 12708. https://doi.org/10.1038/ncomms12708.

75. Ye, J., Cheung, J., Gerbino, V., Ahlsén, G., Zimanyi, C., Hirsh, D., and Maniatis, T. (2019). Effects of ALS-associated TANK binding kinase 1 mutations on protein-protein interactions and kinase activity. Proc. Natl. Acad. Sci. USA *116*, 24517–24526. https://doi.org/10.1073/pnas.1915732116.

76. Shi, X., Yokom, A.L., Wang, C., Young, L.N., Youle, R.J., and Hurley, J.H. (2020). ULK complex organization in autophagy by a C-shaped FIP200 N-terminal domain dimer. J. Cell Biol. *219*. https://doi.org/10.1083/jcb.201911047.

77. Fu, T., Zhang, M., Zhou, Z., Wu, P., Peng, C., Wang, Y., Gong, X., Li, Y., Wang, Y., Xu, X., et al. (2021). Structural and biochemical advances on the recruitment of the autophagy-initiating ULK and TBK1 complexes by autophagy receptor NDP52. Sci. Adv. *7*. https://doi.org/10.1126/sciadv.abi6582.

78. Ryzhakov, G., and Randow, F. (2007). SINTBAD, a novel component of innate antiviral immunity, shares a TBK1-binding domain with NAP1 and TANK. EMBO J. *26*, 3180–3190. https://doi.org/10.1038/sj.emboj.7601743.

79. Thurston, T.L., Ryzhakov, G., Bloor, S., von Muhlinen, N., and Randow, F. (2009). The TBK1 adaptor and autophagy receptor NDP52 restricts the proliferation of ubiquitin-coated bacteria. Nat. Immunol. *10*, 1215–1221. https://doi.org/10.1038/ni.1800.

80. Jung, C.H., Jun, C.B., Ro, S.H., Kim, Y.M., Otto, N.M., Cao, J., Kundu, M., and Kim, D.H. (2009). ULK-Atg13-FIP200 complexes mediate mTOR signaling to the autophagy machinery. Mol. Biol. Cell *20*, 1992–2003. https://doi.org/10.1091/mbc.E08-12-1249.

81. Wold, M.S., Lim, J., Lachance, V., Deng, Z.Q., and Yue, Z.Y. (2016). ULK1-mediated phosphorylation of ATG14 promotes autophagy and is

impaired in Huntington's disease models. Mol. Neurodegener. *11*, 76. https://doi.org/10.1186/s13024-016-0141-0.

82. Chang, C., Shi, X., Jensen, L.E., Yokom, A.L., Fracchiolla, D., Martens, S., and Hurley, J.H. (2021). Reconstitution of cargo-induced LC3 lipidation in mammalian selective autophagy. Sci. Adv. *7*. https://doi.org/10.1126/sciadv.abg4922.
83. Park, J.M., Jung, C.H., Seo, M., Otto, N.M., Grunwald, D., Kim, K.H., Moriarity, B., Kim, Y.M., Starker, C., Nho, R.S., et al. (2016). The ULK1 complex mediates MTORC1 signaling to the autophagy initiation machinery via binding and phosphorylating ATG14. Autophagy *12*, 547–564. https://doi.org/10.1080/15548627.2016.1140293.
84. Jao, C.C., Ragusa, M.J., Stanley, R.E., and Hurley, J.H. (2013). A HORMA domain in Atg13 mediates PI 3-kinase recruitment in autophagy. Proc. Natl. Acad. Sci. USA *110*, 5486–5491. https://doi.org/10.1073/pnas.1220306110.
85. Youle, R.J. (2019). Mitochondria-Striking a balance between host and endosymbiont. Science *365*, 655. https://doi.org/10.1126/science.aaw9855.
86. Yamamoto, H., Kakuta, S., Watanabe, T.M., Kitamura, A., Sekito, T., Kondo-Kakuta, C., Ichikawa, R., Kinjo, M., and Ohsumi, Y. (2012). Atg9 vesicles are an important membrane source during early steps of autophagosome formation. J. Cell Biol. *198*, 219–233. https://doi.org/10.1083/jcb.201202061.
87. Zachari, M., Gudmundsson, S.R., Li, Z., Manifava, M., Cugliandolo, F., Shah, R., Smith, M., Stronge, J., Karanasios, E., Piunti, C., et al. (2019). Selective autophagy of mitochondria on a ubiquitin-endoplasmic-reticulum platform. Dev. Cell *50,* 627–643.e5. https://doi.org/10.1016/j.devcel.2019.06.016.
88. Chan, E.Y.W., Kir, S., and Tooze, S.A. (2007). SiRNA screening of the kinome identifies ULK1 as a multidomain modulator of autophagy. J. Biol. Chem. *282*, 25464–25474. https://doi.org/10.1074/jbc.M703663200.
89. Hosokawa, N., Hara, T., Kaizuka, T., Kishi, C., Takamura, A., Miura, Y., Iemura, S., Natsume, T., Takehana, K., Yamada, N., et al. (2009). Nutrient-dependent mTORC1 association with the ULK1-Atg13-FIP200 complex required for autophagy. Mol. Biol. Cell *20*, 1981–1991. https://doi.org/10.1091/mbc.E08-12-1248.
90. Alers, S., Löffler, A.S., Paasch, F., Dieterle, A.M., Keppeler, H., Lauber, K., Campbell, D.G., Fehrenbacher, B., Schaller, M., Wesselborg, S., et al. (2011). Atg13 and FIP200 act independently of Ulk1 and Ulk2 in autophagy induction. Autophagy *7*, 1423–1433. https://doi.org/10.4161/auto.7.12.18027.
91. Cheong, H., Lindsten, T., Wu, J.M., Lu, C., and Thompson, C.B. (2011). Ammonia-induced autophagy is independent of ULK1/ULK2 kinases. Proc. Natl. Acad. Sci. USA *108*, 11121–11126. https://doi.org/10.1073/pnas.1107969108.
92. Hieke, N., Löffler, A.S., Kaizuka, T., Berleth, N., Böhler, P., Drießen, S., Stuhldreier, F., Friesen, O., Assani, K., Schmitz, K., et al. (2015). Expression of a ULK1/2 binding-deficient ATG13 variant can partially restore autophagic activity in ATG13-deficient cells. Autophagy *11*, 1471–1483. https://doi.org/10.1080/15548627.2015.1068488.
93. Qi, S.Q., Kim, D.J., Stjepanovic, G., and Hurley, J.H. (2015). Structure of the human Atg13-Atg101 HORMA heterodimer: an interaction hub within the ULK1 complex. Structure *23*, 1848–1857. https://doi.org/10.1016/j.str.2015.07.011.
94. Suzuki, H., Kaizuka, T., Mizushima, N., and Noda, N.N. (2015). Structure of the Atg101-Atg13 complex reveals essential roles of Atg101 in autophagy initiation. Nat. Struct. Mol. Biol. *22*, 572–580. https://doi.org/10.1038/nsmb.3036.
95. Ren, X., Nguyen, T.N., Lam, W.K., Buffalo, C.Z., Lazarou, M., Yokom, A.L., and Hurley, J.H. (2023). Structural basis for ATG9A recruitment to the ULK1 complex in mitophagy initiation. Sci. Adv. *9,* eadg2997. https://doi.org/10.1126/sciadv.adg2997.
96. Perez-Riverol, Y., Csordas, A., Bai, J., Bernal-Llinares, M., Hewapathirana, S., Kundu, D.J., Inuganti, A., Griss, J., Mayer, G., Eisenacher, M., et al. (2019). The PRIDE database and related tools and resources in 2019: improving support for quantification data. Nucleic Acids Res. *47,* D442–D450. https://doi.org/10.1093/nar/gky1106.
97. Vijayachandran, L.S., Viola, C., Garzoni, V., Trowitzsch, S., Bieniossek, C., Chaillet, M., Schaffitzel, C., Busso, D., Romier, C., Poterszman, A., et al. (2011). Robots, pipelines, polyproteins: enabling multiprotein expression in prokaryotic and eukaryotic cells. J. Struct. Biol. *175*, 198–208. https://doi.org/10.1016/j.jsb.2011.03.007.
98. Ran, F.A., Hsu, P.D., Wright, J., Agarwala, V., Scott, D.A., and Zhang, F. (2013). Genome engineering using the CRISPR-Cas9 system. Nat. Protoc. *8*, 2281–2308. https://doi.org/10.1038/nprot.2013.143.
99. Neuhold, J., Radakovics, K., Lehner, A., Weissmann, F., Garcia, M.Q., Romero, M.C., Berrow, N.S., and Stolt-Bergner, P. (2020). GoldenBac: a simple, highly efficient, and widely applicable system for construction of multi-gene expression vectors for use with the baculovirus expression vector system. BMC Biotechnol. *20*, 26. https://doi.org/10.1186/s12896-020-00616-z.
100. Schindelin, J., Arganda-Carreras, I., Frise, E., Kaynig, V., Longair, M., Pietzsch, T., Preibisch, S., Rueden, C., Saalfeld, S., Schmid, B., et al. (2012). Fiji: an open-source platform for biological-image analysis. Nat. Methods *9*, 676–682. https://doi.org/10.1038/nmeth.2019.
101. Tyanova, S., Temu, T., and Cox, J. (2016). The MaxQuant computational platform for mass spectrometry-based shotgun proteomics. Nat. Protoc. *11*, 2301–2319. https://doi.org/10.1038/nprot.2016.136.
102. Lazarou, M., McKenzie, M., Ohtake, A., Thorburn, D.R., and Ryan, M.T. (2007). Analysis of the assembly profiles for mitochondrial- and nuclear-DNA-encoded subunits into complex I. Mol. Cell. Biol. *27*, 4228–4237. https://doi.org/10.1128/MCB.00074-07.
103. Yu, C., Zhang, Y., Yao, S., and Wei, Y. (2014). A PCR based protocol for detecting indel mutations induced by TALENs and CRISPR/Cas9 in zebrafish. PLoS One *9,* e98282. https://doi.org/10.1371/journal.pone.0098282.
104. Wurzer, B., Zaffagnini, G., Fracchiolla, D., Turco, E., Abert, C., Romanov, J., and Martens, S. (2015). Oligomerization of p62 allows for selection of ubiquitinated cargo and isolation membrane during selective autophagy. eLife *4,* e08941. https://doi.org/10.7554/eLife.08941.

STAR★METHODS

KEY RESOURCES TABLE

REAGENT or RESOURCE	SOURCE	IDENTIFIER
Antibodies		
Mouse anti-COXII	Abcam	Cat# ab110258; RRID: AB_10887758
Mouse anti-HSP60	Abcam	Cat# ab128567; RRID: AB_11145464
Mouse anti-WIPI2	Abcam	Cat# ab105459; RRID: AB_10860881
Mouse anti-Actin	Cell Signaling	Cat# 4967S; RRID: AB_330288
Mouse anti-HA	Cell Signalling	Cat# 2367; RRID: AB_10691311
Rabbit anti-ATG13	Cell Signaling	Cat# 13468; RRID: AB_2797419
Rabbit anti-ATG13(S355)	Cell Signaling	Cat#46329S
Rabbit anti-ATG14(S29)	Cell Signaling	Cat# 92340S; RRID: AB_2800182
Rabbit anti-ATG14	Cell Signaling	Cat# 96752S; RRID: AB_2737056
Rabbit anti-FIP200	Cell Signaling	Cat# 12436S; RRID: AB_2797913
Rabbit anti-HA	Cell Signaling	Cat# 3724S; RRID: AB_1549585
Rabbit anti-TBK1	Cell Signalling	Cat# 38066;RRID: AB_2827657
Rabbit anti-TBK1(S172)	Cell Signalling	Cat# 5483; RRID: AB_10693472
Rabbit anti-ULK1	Cell Signaling	Cat# 8054S; RRID: AB_11178668
Rabbit anti-ULK1(S317)	Cell Signaling	Cat# 37762S; RRID: AB_10831845
Rabbit anti-VCP	Cell Signaling	Cat# 2649; RRID: AB_2214629
Mouse anti-Halo	Promega	Cat# G9211; RRID: AB_2688011
Rabbit anti-OPTN	Proteintech	Cat# 10837-1-AP;RRID: AB_2156665
Mouse anti-Parkin	Santa Cruz	Cat# sc-32282; RRID: AB_628104
Chicken anti-GFP	ThermoFisher	Cat# A10262; RRID: AB_2534023
Alexa Fluor 488 goat anti-rabbit IgG (H+L)	Thermofisher	Cat# A11008; RRID: AB_143165
Alexa Fluor 555 goat anti-rabbit IgG (H+L)	Thermofisher	Cat# A21428; RRID: AB_2535849
Alexa Fluor 647 goat anti-rabbit IgG (H+L)	Thermofisher	Cat# A21244; RRID: AB_2535812
Alexa Fluor 488 goat anti-mouse IgG (H+L)	Thermofisher	Cat# A21202; RRID: AB_141607
Alexa Fluor 555 goat anti-mouse IgG (H+L)	Thermofisher	Cat# A21422; RRID: AB_2535844
Alexa Fluor 647 goat anti-mouse IgG (H+L)	Thermofisher	Cat# A21235; RRID: AB_2535804
Chemicals, peptides, and recombinant proteins		
Oligomycin	Calbiochem	495455
Antimycin A	Sigma	A8674
QVD	MedChemExpress	HY-12305
BX795	Enzo Life Sciences	ENZ-CHM189-0005
Lipofectamine LTX	Life Technologies	A12621
X-tremeGENE 9	Roche	6365787001
TMR-conjugated Halo ligand	Promega	G8251
Pierce™ anti-HA magnetic beads	Thermofisher	88836
NEBuilder HiFi DNA assembly	New England Biolabs	E2621L
Deposited data		
MS proteomics data	This paper (Figure S8A)	ProteomeXchange Consortium via the PRIDE partner repository[96] with the dataset identifier PXD039663 (PRIDE: PXD039663)
The original data for this study	This paper	Zenodo: https://doi.org/10.5281/zenodo.7902562

(*Continued on next page*)

Continued

REAGENT or RESOURCE	SOURCE	IDENTIFIER
Experimental models: Cell lines		
Penta KO HeLa cells	Lazarou et al.[41]	RRID: CVCL_C2VN
ATG13 KO/penta KO HeLa cells	This paper	RRID: CVCL_C2VP
ATG14 KO/penta KO HeLa cells	This paper	RRID: CVCL_C2VQ
TBK1 KO/penta KO HeLa cells	This paper	RRID: CVCL_C2VR
ULK1/2 DKO/penta KO HeLa cells	This paper	RRID: CVCL_C2VS
TBK1/ULK1/2 TKO/penta KO HeLa cells	This paper	RRID: CVCL_C2VT
HEK293T	ATCC	Cat# CRL-3216; RRID:CVCL_0063
Wild type HeLa cells	ATCC	Cat# CCL-2.2; RRID: CVCL_0058
Sf9 cells	ThermoFisher Scientific	Cat# 12659017; RRID:CVCL_0549
Free style 293-F cells	ThermoFisher Scientific	Cat# R79007; RRID: CVCL_D603
DH10BACY	Vijayachandran et al.[97]	N/A
Oligonucleotides		
ULK1 (genotyping) F	GCGCGGATCCCTGCGCCATGGAGCCCGG	N/A
ULK1 (genotyping) R	GCGCAAGCTTGGGACAGGCGGGGAATCTCG	N/A
ULK2 (genotyping) F	TGCATATTTCAAATCCTTTTTGAT	N/A
ULK2 (genotyping) R	ACAACAACAACAACTGGTCTGC	N/A
ULK2 sequencing primer	GATTCAGTGATCTAGATTC	N/A
TBK1 (genotyping) F	CGAAAACTACATTACAGATTTTGCC	N/A
TBK1 (genotyping) R	ACCACAAAATCACTTGGAAAGG	N/A
TBK1 sequencing primer	GCTCTATAAAGGATAAAG	N/A
ATG13 (genotyping) F	TGAGATTTGGGGCTTTGATGC	N/A
ATG13 (genotyping) R	TGACCCCCTCAGAGAATGAT	N/A
ATG13 sequencing primer	AGAGTGTGAGGAGCCTTCAGT	N/A
ATG14 (genotyping) F	GAAAACAAAATCCCACGTGACT	N/A
ATG14 (genotyping) R	AGCAGCTAGCTACACTCCCTCT	N/A
ATG14 sequencing primer	GAGGACACACAGCAGAA	N/A
Recombinant DNA		
pBMN-BFP-Parkin	Nguyen et al.[15]	Addgene #186221
pSpCas9(BB)-2A-GFP vector	Ran et al.[98]	Addgene #48138
pCHAC-mt-mKeima	Lazarou et al.[41]	Addgene #72342
pSu9-HaloTag7-mGFP	Yim et al.[72]	Addgene #184905
pBMN-HA-ATG13	Ren et al.[95]	Addgene #186223
pBMN-HA-ATG13$^{\Delta HORMA}$	Ren et al.[95]	Addgene #186222
pBMN-HA-NDP52	This paper	Addgene #199307
pBMN-HA-TBK1	This paper	Addgene #199205
pBMN-HA-TBK1^{KD}	This paper	Addgene #199206
pBMN-HA- TBK1^{E696K}	This paper	Addgene #199207
pBMN-GFP-NDP52	Lazarou et al.[41]	Addgene #188785
pBMN-GFP-OPTN	Lazarou et al.[41]	Addgene #188784
pGEM4Z	Promega	Cat# P2161
pGB	Neuhold et al.[99]	N/A
Expression constructs for protein purification	Table S2	N/A
Software and algorithms		
FIJI (ImageJ); Version 1.52q	Schindelin et al[100] (https://imagej.nih.gov/ij/)	RRID:SCR_002285
ImageJ	https://imagej.nih.gov/ij/	RRID:SCR_003070
Prism	GraphPad	RRID:SCR_002798

(*Continued on next page*)

Continued

REAGENT or RESOURCE	SOURCE	IDENTIFIER
Image Lab software; Version 6.0	BioRad Laboratories	RRID:SCR_014210
FlowJo (version 10)	FlowJo	RRID:SCR_008520
MaxQuant (version 2.0.3.0)	Tyanova et al.[101]	RRID:SCR_014485
Leica Application Suite X (LASX v2.0.1)	Leica Microsystems	RRID:SCR_013673
Uniprot Spodoptera frugiperda reference proteome (version 2021.04)	www.uniprot.org	N/A
Plugin – 3D ROI manager (v3.93)	http://imagejdocu.tudor.lu/doku.php?id=plugin:stacks:3d_roi_manager:start	RRID:SCR_017065
FACSDiva software	http://www.bdbiosciences.com/instruments/software/facsdiva/index.jsp	RRID:SCR_001456
R (Ver.>4.2)	http://www.r-project.org/	RRID:SCR_001905

RESOURCE AVAILABILITY

Lead contact

Further information and requests for resources and reagents should be directed to and will be fulfilled by the Lead Contact, Michael Lazarou (Lazarou.m@wehi.edu.au).

Materials availability

All unique/stable reagents generated in this study are available from the Lead Contact with a completed Materials Transfer Agreement.

Data and code availability

- All data generated in this study, including electron micrographs, confocal microscopy images, and immunoblots, have been deposited and are publicly available as of the date of publication. Accession numbers and DOI are listed in the key resources table.
- This paper does not report original code.
- Any additional information required to reanalyze the data reported in this paper is available from the lead contact upon request.

EXPERIMENTAL MODEL AND SUBJECT DETAILS

Cell lines in this study (HeLa cell lines and HEK293T) were cultured Dulbecco's modified eagle medium (DMEM) supplemented with 10 % (v/v) FBS (Cell Sera Australia), 1 % Penicillin-Streptomycin, 25 mM HEPES, 1x GlutaMAX (Life Technologies) and 1x non-essential amino acids (Life Technologies).

METHOD DETAILS

Antibodies and reagents

The monoclonal and polyclonal antibodies used in this study are listed in key resources table. The polyclonal B17.2L antibody (a kind gift from Prof. Mike Ryan (Monash University)) was previously generated in rabbits using recombinant full length B17.2L antigen.[102]

Generation of knockout lines using CRISPR/Cas9 gene editing

Penta KO cells were described previously.[41] All knockout cell lines in this study are CRISPR/Cas9-edited cell lines. CRISPR guide RNAs (gRNAs) that target a common exon of all splicing variants of each gene of interest were incorporated into oligonucleotides (Sigma) and introduced into BbsI-linearised pSpCas9(BB)-2A-GFP vector (a gift from Feng Zhang; Addgene #48138) using Gibson Cloning kit (New England Biolabs). The protocol is available here https://doi.org/10.17504/protocols.io.j8nlkkzo6l5r/v1. gRNA constructs were then sequence-verified and transfected into penta KO cells with X-tremeGENE 9 (Roche) overnight and single cells that were positive for GFP were sorted by fluorescence activated cell sorting (FACS) into 96 well plates. Single cell colonies were then expanded and collected for screening by immunoblotting for the loss of the targeted gene product. Once the knockout cell lines were identified, gene editing was detected using Sanger sequencing. The CRISPR-targeted regions were amplified via PCR and PCR products were sequenced using sequencing primers that anneal to the amplified regions (key resources table). For analysis purpose, the same regions in the parental line were also sequenced. Synthego ICE v2 CRISPR Analysis Tool

(synthego.com/products/bioinformatics/crispr-analysis) was used to compare the sequencing data from the control and the knockout cells, allowing the identification of gene edits in the knockout cells (Table S1). For *ULK1* KO cell lines (in *ULK1/2* DKO/penta KO and *TBK1/ULK1/2* TKO/penta; Table S1), sequencing the amplified PCR products appeared to be difficult, we therefore cloned them into a pGEM4Z vector (Promega; Cat# P2161) prior to sequencing analysis (see key resources table for details of genotyping primers). Although the sequencing reads were not of high quality in some parts, there was a clear edit of 10 bp deletion at the CRISPR target region which resulted in frameshift and premature stop codon (Table S1). Nevertheless, there was no protein detected by immunoblotting (Figure 1A). Where antibodies were not available, putative KO clones were first identified by three primer PCR[103] and the presence of frameshift indels was determined by Sanger sequencing. The protocol is available online https://doi.org/10.17504/protocols.io.8epv59yx5g1b/v1. Multiple knockout lines were generated by sequential transfections of one or multiple gRNA constructs. For *ULK1/2* DKO/penta KO, ULK1 CRISPR was transfected into penta KO cells to make *ULK1* KO/penta KO. The introduction of ULK2 CRISPR into *ULK1* KO/penta KO produced *ULK1/2* DKO/penta KO. Subsequent editing of *ULK1/2* DKO/penta KO with TBK1 CRISPR generated *TBK1/ULK1/2* TKO/penta KO.

Cloning and generation of stable cell lines

pBMN-mEGFP-OPTN (Addgene #188784), pBMN-mEGFP-NDP52 (Addgene #188785), pBMN-BFP-Parkin (Addgene #186221) and universal vector backbones pBMN-mEGFP (Addgene #188643), pBMN-HA-C1 (Addgene #188645) and pBMN-BFP-C1 (Addgene #188644) was previously described.[15,56] Open reading frames (ORFs) of ATG13, ATG13$^{\Delta 1\text{-}198}$ referred to as ATG13$^{\Delta HORMA}$, NDP52, TBK1, TBK1^{D135N} referred to as kinase dead (KD) TBK1 (TBK1^{KD}), TBK1^{E696K} were introduced into linearised pBMN-HA-C1 using Gibson Cloning kit (New England Biolabs) to create pBMN-HA-ATG13, -ATG13$^{\Delta HORMA}$, -NDP52, -TBK1, -TBK1^{KD}, TBK1^{E696K}. All constructs were sequence-verified.

Stable cell lines were generated using retroviral system as described previously.[15] First, a retroviral vector (pCHAC-mito-Keima and all pBMN constructs) containing an ORF of interest and retroviral packaging plasmids (VSV-G and Gag-Pol) were transfected into HEK293T cells using Lipofectamine LTX (Life Technologies) for 15 h. The next day, the transfection media was replaced with fresh growing DMEM to allow the assembly and secretion of retroviruses. After 24 h incubation, supernatant containing retroviruses was collected, filtered, and applied onto the desired HeLa cells for 24-48 h in the presence 8 mg/ml polybrene (Sigma). Cells were then recovered and expanded in growing DMEM for 5-7 days prior to sorting by FACS to match protein expression levels where possible. The protocol for generating stable cell lines is available at https://doi.org/10.17504/protocols.io.dm6gpjzm8gzp/v1.

Mitophagy treatment and immunoblotting

Translocation and mitophagy experiments were achieved by incubating cells with 10 μM Oligomycin (Calbiochem), 4 μM Antimycin A (Sigma) and 10 μM QVD (ApexBio) in full growth medium for different time points as indicated in figure legends. For the analysis of BX795 treatment, the indicated samples were pre-treated for 30 min with 1 μM BX795 in growth media before inducing mitophagy in the presence of 1μM BX795.

For Western blot analysis, cells from 6 well plates were washed with 1x PBS, harvested using cell scrapers and lysed in 1× LDS sample buffer (Life Technologies) supplemented with 100 mM dithiothreitol (DTT; Sigma). Samples were heated at 99 °C with shaking for 7-10 min. Approximately 25-80 μg of protein per sample was analysed by 4-12% Bis-Tris gels (Life Technologies) according to manufacturer's instructions. Gels were electro-transferred to polyvinyl difluoride membranes (PVDF) and immunoblotted using indicated antibodies. The protocol is deposited here https://doi.org/10.17504/protocols.io.kxygxzxr4v8j/v1

Immunoprecipitation with anti-HA magnetic beads

Cells were lysed in lysis buffer containing 50mM Tris-Cl (pH 7.5 when cold), 150mM NaCl, 0.5 % TX-100 supplemented with 1x cOmplete, EDTA-free protease inhibitor cocktail (Roche) and 0.1 μl of benzonase (Sigma) and incubate samples on ice for 30 min. Anti-HA magnetic beads (Pierce) were washed three times with 50mM Tris-Cl (pH 7.5 when cold), 150mM NaCl, 0.1% Tween20. Cell lysates were centrifuged at max speed for 10 min at 4 °C. The supernatants were then diluted with 50mM Tris-Cl (pH 7.5 when cold), 150mM NaCl, 1x cOmplete, EDTA-free protease inhibitor cocktail so that the concentration of TX-100 is at 0.17 % and incubated with anti-HA magnetic beads. Following a 3 h incubation on a rotary mixer at 4 °C, beads were washed with 50mM Tris-Cl (pH 7.5 when cold), 150mM NaCl, 0.1 % TX-100, 1x cOmplete, EDTA-free protease inhibitor cocktail and bound proteins were eluted by boiling beads in 1X LDS containing 100 mM DTT at 99 °C for 10 min. Samples were immunoblotted as described in mitophagy treatment and immunoblotting section. The detailed protocol is available online https://doi.org/10.17504/protocols.io.eq2ly79yelx9/v1

IMMUNOFLUORESCENCE ASSAY AND CONFOCAL IMAGE ANALYSIS

For immunofluorescence, 48 h before treatment cells were seeded on HistoGrip (ThermoFisher) coated glass coverslips for. All following steps were performed at room temperature. Samples were first fixed with 4% (w/v) paraformaldehyde (PFA) in 0.1 M phosphate buffer on a rocker for 10 min. Samples were then rinsed three times with 1x PBS, permeabilized with 0.1% (v/v) Triton X-100 in 1x PBS (10 min) and then blocked with 3% (v/v) goat serum in 0.1% (v/v) Triton X-100/1x PBS (15 min). The samples were incubated with indicated primary antibodies made up in 3 % (v/v) goat serum in 0.1 % (v/v) Triton X-100/1x PBS for 90 min and rinsed three times with 1x PBS. Following 1 h incubation with secondary antibodies conjugated to AlexaFluor-488, Alexa-Fluor-555, AlexaFluor-633, or

AlexaFluor-647 (ThermoFisher), the coverslips were washed three times with 1x PBS and mounted with a TRIS buffered DABCO-glycerol mounting medium onto glass slides. Imaging of the coverslips wwas done with an inverted Leica SP8 confocal laser scanning microscope under 63x/1.40NA objective (Oil immersion, HC PLAPO, CS2; Leica microsystems). Images were acquired in 3D by optical sectioning using an with a minimum z-stack range of 1.8 μm and a maximum voxel size of 90 nm laterally (x,y) and 300 nm axially (z) using a Leica HyD Hybrid Detector (Leica Microsystems) and the Leica Application Suite X (LASX v2.0.1; https://www.leica-microsystems.com/products/microscope-software/details/product/leica-las-x-ls/). All images are displayed as z-stack maximum projections. For image analysis, three images were taken per sample at random stage positions. If the field-of -view of any image contained less than 30 cells, another random one was chosen for imaging. The protocol is described here https://doi.org/10.17504/protocols.io.5qpvobz99l4o/v1

Automated 3D image segmentation approach with 3D ROI manager (v3.93) and FeatureJ (v3.0.0) plugins for FIJI (v1.52p) was employed to process and analyse all 3D image data. As described previously,[56] the image analysis process includes three steps: object detection, object measurement and analysis. To account for the lack of foci in the untreated conditions, ATG13 and WIPI2b foci were detected and segmented using a global thresholding strategy. For each experiment repeat, a montage of maximum intensity projections of all images was assembled, and new minimum and maximum intensity values required for linear histogram normalization of that montage were calculated. The minimum and maximum intensity values were defined if the number of pixels at a given intensity exceeded 0.02 % of all pixels in the montage. The histogram of each individual image was then rescaled between these new maximum and minimum values to generate normalized data. This data was then subjected to 3D noise filtering (3D median filter; 1.5 voxels) and extraction of 3D ROIs using a global threshold (ATG13 and WIPI2b, 64; arbitrary) via simple 3D thresholding (300 voxel maximum size). Re-applying each extracted 3D ROI to the original corresponding image allowed the determination of volumes and fluorescence intensities for each segmented object in all available channels. All the measurements and ROIs were saved for subsequent analyses. Foci volume and number for ATG13 and WIPI2b were calculated by direct measurement of these parameters from the 3D ROIs. The number of cells in each image was counted manually.

Mito-Keima autophagosome-lysosome fusion mitophagy assay

Cells were seeded into 24 well plates one day before the experimental day. Following mitophagy induction at indicated time points, cells were washed with 1x PBS, detached with trypsin (Life Technologies) and harvested in normal growth media. Samples were then centrifuged at 4 °C and resuspended in ice cold sorting buffer containing 10 % v/v FBS and 0.5 mM EDTA in 1x PBS). Samples were analysed using the FAVSDiva software on a LSR Fortessa X-20 cell sorter (BD Biosciences). Lysosomal mtKeima was measured using dual excitation ratiometric pH measurements at 488 (pH 7) and 561 (pH 4) nm lasers with 695 nm and 670 nm detector filters respectively. Additional channel used was GFP (Ex/Em; 488 nm/530 nm) for fluorescence compensation. For each sample, 30,000 events were collected, and data were analysed using FlowJo (version 10). The protocol is deposited online https://doi.org/10.17504/protocols.io.q26g74e1qgwz/v1.

Halo assay to assess mitophagy flux

Halo mitophagy assay was recently developed.[72] The protocol is described in detail here https://dx.doi.org/10.17504/protocols.io.dm6gpjzm8gzp/v1. Cells stably expressing mitochondrially targeted Halo tagged protein using pSu9-Halo-mGFP construct (Addgene, no. 184905) were seeded into 6 well plates and left growing overnight. The next day, cells were incubated with growth media containing 50 nM TMR-conjugated Halo ligand (Promega). After 20 min incubation, the cells were then washed twice with 1x PBS. Untreated samples were harvested while mitophagy-induced samples were treated as described in mitophagy treatment and immunoblotting section for 6 h. Following treatment, the cells were washed with ice-cold 1x PBS, harvested, and analysed via immunoblotting.

Transmission electron microscopy imaging

Samples for transmission electron microscope (TEM) analysis were fixed with pre-warmed 4 % PFA in 0.1 M phosphate buffer (pH 7.2) at 37 °C for 1 hour followed by overnight post-fixation with 2.5 % glutaraldehyde in 0.1 M sodium cacodylate buffer (pH 7.4) at 4 °C. Samples were rinsed three times with 0.1 M sodium cacodylate buffer. All subsequent sample preparation steps were microwave assisted using a BioWave Pro microwave system (Pelco). The samples were osmicated with 1 % (w/v) OsO4, 1.5 % (w/v) K3Fe(CN)6 in 0.1 M cacodylate buffer for 1 hour at 4 °C, before exposure to three microwave duty-cycles (120 s on, 120 s off) at 100 W under vacuum. The samples were rinsed three times with MilliQ water and en bloc stained with 2 % (w/v) aqueous uranyl acetate with three 100 W microwave duty-cycles (120 s on, 120 s off) under vacuum. Samples were then rinsed with MilliQ water twice before the cells were scraped, resuspended in 500 μL MilliQ, and pelleted (10,000x g). The cells were then repelleted in 500 μL 70% ethanol, and further resuspended and pelleted in 300 μL low-melting point agarose at 37°C. The solidified agarose-cell pellet was divided into 1 mm cubes using a razor blade for subsequent processing. Microwave assisted dehydration was performed by graduated ethanol series (80 %, 90 %, 95 %, 100 %, 100 % (v/v); each at 150 W for 40 s) and propylene oxide (100 %, 100 % (v/v); each at 150 W for 40 s). The samples were infiltrated with Araldite 502/Embed 812 by graduated concentration series in propylene oxide (25 %, 50 %, 75 % 100 %, 100 % (v/v); 180 s at 250 W under vacuum), then polymerized at 60 °C for two days. Ultracut UCT ultramicrotome (Leica Biosystems) equipped with a 45 °C diamond knife (Diatome) was used to section the resin embedded samples, and 75 nm ultrathin sections were collected and loaded on 75 mesh copper grids. The grids were stained at room temperature using 2 % (w/v) aqueous

uranyl acetate (5 min) and Reynolds lead citrate (3 min) before routine imaging on a JEM-1400PLUS TEM (JEOL). Cells were imaged by acquiring a montage of high magnification (5,000X) images and the visible autophagosomal structures were further imaged at 10,000X magnification for validation. The protocol is deposited here https://doi.org/10.17504/protocols.io.14egn75zmv5d/v1

Protein expressions and purification

Linear tetra-ubiquitin (GST-4xUb), the GFP-ULK1 complex and FIP200-GFP were expressed and purified as previously described.[39,71,104] The protocols are deposited online (GST-4xUb: https://doi.org/10.17504/protocols.io.bvjbn4in; GFP-ULK complex: https://doi.org/10.17504/protocols.io.bvn2n5ge; FIP200-GFP: https://doi.org/10.17504/protocols.io.dm6gpbkq5lzp/v1)

The pGST2-GST-TEV-OPTN, pGST2-GST-TEV-OPTN(S177D S473D) and pGST2-GST-TEV-NDP52 constructs were generated by introducing TEV cleavage site to corresponding vectors[82] (Protocol: https://doi.org/10.17504/protocols.io.bp2l61znrvqe/v1). The proteins were expressed in *E. coli* Rosetta pLySS cells. Cells were grown in LB medium at 37°C until an OD600 of 0.4 and then at 18°C until an OD600 of 0.8. Protein expression was induced with 100 μM IPTG for 16 h at 18°C. Cells were pelleted and resuspended in a buffer containing 50 mM HEPES, pH 7.5, 300 mM NaCl, 2 mM MgCl2, 2 mM β-mercaptoethanol, cOmplete protease inhibitors (Roche), and DNase. Cells were lysed by freeze thawing and 2 × 30 s sonication. Lysates were cleared by ultracentrifugation (25,000 rpm for 30 min at 4°C). Supernatant was incubated with 5 ml Glutathione Sepharose 4B beads slurry (Cytiva) for 1h at 4°C. Beads were then washed with low salt (50 mM HEPES, pH 7.5, 300 mM NaCl, and 1 mM DTT) buffer, followed by high salt (50 mM HEPES, pH 7.5, 500 mM NaCl, and 1 mM DTT) and low salt buffers. Finally, beads were incubated overnight with TEV protease at 4°C. The supernatant containing cleaved protein was filtered through a 0.45 μm syringe filter, concentrated down to 0.5 ml and applied onto a Superdex 200 column (10/300 Cytiva) pre-equillibrated with a buffer containing 25 mM HEPES, pH 7.5, 150 mM NaCl, and 1 mM DTT. Fractions containing pure proteins were pooled, concentrated, snap frozen in liquid nitrogen, and stored at −80°C.

The mCherry-NDP52 gene coding sequence was cloned in a pET-Duet1 vector, with a N-terminal 6xHis tag followed by a TEV cleavage site. The protein was expressed in *E. coli* Rosetta pLySS cells. Cells were grown in LB medium at 37°C until an OD600 of 0.4 and then at 18°C until an OD600 of 0.8. Protein expression was induced with 50 μM IPTG for 16 h at 18°C. Cells were pelleted and resuspended in a buffer containing 50mM HEPES pH7.5, 300 mM NaCl, 1 mM MgCl2, 10 mM Imidazole, 2 mM Beta-Mercaptoethanol, cOmplete protease inhibitors (Roche), and DNase (Sigma). Cells were lysed by freeze thawing and 3 × 30 s sonication. Lysates were cleared by ultracentrifugation (40,000 rpm for 45 min at 4°). Supernatant was filtered (0.45 μm), applied to a 5-ml His-Trap HP column and eluted via a stepwise imidazole gradient (50, 75, 100, 150, 200, and 300 mM). Fractions at 75–100 mM imidazole containing His-TEV-mCh-NDP52 were pooled and subjected to TEV protease cleavage over night at 4°C. The cleaved protein was concentrated using a 50kDa cut-off Amicon filter and injected to a Superdex200 16/600 column (Cytiva) and eluted with a buffer containing 25mM HEPES pH7.5, 150mM NaCl, 1mM DTT. Purified protein was concentrated, snap frozen in liquid nitrogen, and stored at −80°C. The protocol is deposited online (https://doi.org/10.17504/protocols.io.5qpvobdr9l4o/v1)

To generate GFP-TBK1 constructs the insect codon optimized TBK1 gene was purchased from GenScript and cloned with respective tags into pFastBac_Dual (Table S2). Generated constructs were used for expression in Sf9 insect cells using the Bac-to-Bac system. The bacmid DNAs (2.5 μg per construct), obtained by amplification in DH10BacY cells were used to transfect Sf9 insect cells using FuGene transfection reagent (Promega). About 7 days after transfection the V0 virus was harvested and used to produce a V1 virus stock, which in turn was used to infect 1 L Sf9 cells (1 million/ml) for protein expression. After infection cells were monitored and harvested by centrifugation when they reached a viability of 95%–98%. Cell pellets were washed with PBS, flashfrozen in liquid nitrogen, and stored at −80 °C until purification. For purification of GFP-TBK1, a cell pellet corresponding to 1L culture was thawed and resuspended in 30 ml lysis buffer (50 mM Tris-HCl pH 7.4, 300mM NaCl, 2 mM MgCl2, 5% glycerol, 2 mM β-Met, 1 μl Benzonase (Sigma), CIP protease inhibitor (Sigma), cOmplete EDTA-free protease inhibitor cocktail (Roche)). Cells were additionally disrupted with Dounce homogenizer. Lysates were cleared by centrifugation (19 000 rpm for 45 min at 4°C in a Fiberlite F21-8x50y (Thermo Scientific). Supernatant was incubated with 5 ml Glutathione Sepharose 4B beads slurry (Cytiva) for 2h at 4°C. Then beads were washed five times with 50 mM Tris-HCl pH 7.4, 300 mM NaCl, 5% glycerol, 1 mM DTT and incubated overnight with TEV protease at 4°C. The supernatant containing cleaved protein was filtered through a 0.45 μm syringe filter, concentrated down to 0.5 ml and applied onto a Superdex 200 column (10/300, Cytiva) pre-equillibrated with a buffer containing 20 mM Tris-HCl pH 7.4, 300 mM NaCl, and 1 mM DTT. Fractions containing pure proteins were pooled, concentrated, snap frozen in liquid nitrogen, and stored at -80°C. The protocol is available at https://doi.org/10.17504/protocols.io.81wgb6wy1lpk/v1

To generate GST-TEV-SINTBAD-GFP constructs the insect codon optimized SINTBAD gene was purchased from GenScript and cloned with respective tags into pFastBac_Dual (Table S2). Generated constructs were used for expression in Sf9 insect cells using the Bac-to-Bac system. The bacmid DNAs (2.5 μg per construct), obtained by amplification in DH10BacY cells were used to transfect Sf9 insect cells using FuGene transfection reagent (Promega). About 7 days after transfection the V0 virus was harvested and used to produce a V1 virus stock, which in turn was used to infect 1 L Sf9 cells (1 million/ml) for protein expression. After infection cells were monitored and harvested by centrifugation when they reached a viability of 90–95 %. Cell pellets were washed with PBS, flashfrozen in liquid nitrogen, and stored at −80 °C until purification. For purification of SINTBAD-GFP, a cell pellet corresponding to 1L culture was thawed and resuspended in 25 ml lysis buffer (50 mM Tris-HCl pH 8.0, 300mM NaCl, 2 mM MgCl2, 5% glycerol, 2 mM β-Met, 1 μl Benzonase (Sigma), CIP protease inhibitor (Sigma), cOmplete EDTA-free protease inhibitor cocktail (Roche)). Cells were additionally disrupted with Dounce homogenizer. Lysates were cleared by centrifugation (19 000 rpm for 45 min at 4°C in a Fiberlite F21-8x50y

(Thermo Scientific). Supernatant was incubated with 2 ml Glutathione Sepharose 4B beads slurry (Cytiva) for 2h at 4°C. Then beads were washed two times with 50 mM Tris-HCl pH 8.0, 300 mM NaCl, 5% glycerol, 1 mM DTT (Wash Buffer I), once with 50 mM Tris-HCl pH 8.0, 700 mM NaCl, 5% glycerol, 1 mM DTT (Wash Buffer II) and again two times with Wash Buffer I. Washed beads were incubated overnight with TEV protease at 4 °C. The supernatant containing cleaved protein was filtered through a 0.45 μm syringe filter, concentrated down to 0.5 ml and applied onto a Superdex 200 column (10/300, Cytiva) pre-equillibrated with a buffer containing 20 mM Tris-HCl pH 7.4, 150 mM NaCl, and 1 mM DTT. Fractions containing pure proteins were pooled, concentrated, snap frozen in liquid nitrogen, and stored at -80°C.

To generate GST-TEV-SINTBAD-GFP constructs the insect codon optimized SINTBAD gene was purchased from GenScript and cloned with respective tags into pFastBac_Dual (Table S2). Generated constructs were used for expression in Sf9 insect cells using the Bac-to-Bac system. The bacmid DNAs (2.5 μg per construct), obtained by amplification in DH10BacY cells were used to transfect Sf9 insect cells using FuGene transfection reagent (Promega). About 7 days after transfection the V0 virus was harvested and used to produce a V1 virus stock, which in turn was used to infect 1 L Sf9 cells (1 million/ml) for protein expression. After infection cells were monitored and harvested by centrifugation when they reached a viability of 90–95 %. Cell pellets were washed with PBS, flashfrozen in liquid nitrogen, and stored at −80 °C until purification. For purification of SINTBAD-GFP, a cell pellet corresponding to 1L culture was thawed and resuspended in 25 ml lysis buffer (50 mM Tris-HCl pH 8.0, 300mM NaCl, 2 mM MgCl2, 5% glycerol, 2 mM β-Met, 1 μl Benzonase (Sigma), CIP protease inhibitor (Sigma), cOmplete EDTA-free protease inhibitor cocktail (Roche)). Cells were additionally disrupted with Dounce homogenizer. Lysates were cleared by centrifugation (19 000 rpm for 45 min at 4°C in a Fiberlite F21-8x50y (Thermo Scientific). Supernatant was incubated with 2 ml Glutathione Sepharose 4B beads slurry (Cytiva) for 2h at 4°C. Then beads were washed two times with 50 mM Tris-HCl pH 8.0, 300 mM NaCl, 5% glycerol, 1 mM DTT (Wash Buffer I), once with 50 mM Tris-HCl pH 8.0, 700 mM NaCl, 5% glycerol, 1 mM DTT (Wash Buffer II) and again two times with Was Buffer I. Washed beads were incubated overnight with TEV protease at 4 °C. The supernatant containing cleaved protein was filtered through a 0.45 μm syringe filter, concentrated down to 0.5 ml and applied onto a Superdex 200 column (10/300, Cytiva) pre-equillibrated with a buffer containing 20 mM Tris-HCl pH 7.4, 150 mM NaCl, and 1 mM DTT. Fractions containing pure proteins were pooled, concentrated, snap frozen in liquid nitrogen, and stored at -80°C. The protocol is available at https://doi.org/10.17504/protocols.io.rm7vzb1o8vx1/v1.

For NAP1-mCherry, the gene coding for the protein sequence of human NAP1 was subcloned together with N-terminal GST-TEV and C-terminal mCherry tags into a pCAGG by the Vienna BioCenter Core Facilities (VBCF) Protech Facility. The protein was expressed in FreeStyle™ 293-F Cells by transient transfection. The cells grown at 37°C in FreeStyle™ 293 Expression Medium (Thermo, 12338-026) were seeded to density of 0.7 x 10^6 cells per ml the day before transfection. On the day of transfection, 400 ml culture at density of 1x10^6 cells per ml was transfected by addition of vortexed transfection mixture. The mixture consisted of two components: 400 ug of the MAXI-prep DNA that was pre-diluted in 13 ml of Opti-MEMR I Reduced Serum Medium (Thermo, 31985-062) and 800 ug Polyethylenimine (PEI 25K, Polysciences CatNo 23966-1) likewise pre-diluted in 13 ml of Opti-MEM media. 24 hours post transfection, the culture was fed by addition of 100 ml of EXCELL R 293 Serum-Free Medium (SigmaAldrich, 14571C-1000ML). 24H post transfection, the cells were harvested by centrifugation at 270 g for 20 minutes, washed by 1xPBS and flash-frozen in liquid nitrogen prior to storage at -80 °C.

For purification of NAP1-mCh, a cell pellet corresponding to 1L culture was thawed and resuspended in 25 ml lysis buffer (50 mM Tris-HCl pH 8.0, 300mM NaCl, 2 mM MgCl2, 5% glycerol, 2 mM β-Met, 1 μl Benzonase (Sigma), CIP protease inhibitor (Sigma), cOmplete EDTA-free protease inhibitor cocktail (Roche)). Cells were additionally disrupted with Dounce homogenizer and 2 x 30 s sonication. Lysates were cleared by centrifugation (10 000 rpm for 45 min at 4°C in a Fiberlite F21-8x50y (Thermo Scientific). Supernatant was incubated with 2 ml Glutathione Sepharose 4B beads slurry (Cytiva) for 2h at 4°C. Then beads were washed two times with 50 mM Tris-HCl pH 8.0, 300 mM NaCl, 5% glycerol, 1 mM DTT (Wash Buffer I), once with 50 mM Tris-HCl pH 8.0, 700 mM NaCl, 5% glycerol, 1 mM DTT (Wash Buffer II) and again two times with Was Buffer I. Washed beads were incubated overnight with TEV protease at 4 °C. The supernatant containing cleaved protein was filtered through a 0.45 μm syringe filter, concentrated down to 0.5 ml and applied onto a Superose 6 Increase column (10/300, Cytiva) pre-equillibrated with a buffer containing 20 mM Tris-HCl pH 7.4, 300 mM NaCl, and 1 mM DTT. Fractions containing pure proteins were pooled, concentrated, snap frozen in liquid nitrogen, and stored at -80°C. The protocol is available at https://doi.org/10.17504/protocols.io.5jyl8jw6dg2w/v1.

Genes coding for protein sequences of human ATG14, BECN1, VPS34, VPS15 were codon optimized for the Sf9 insect cell expression system, and synthetic genes were purchased from GenScript. All four ORFs were insertent to a GoldenBac plasmid (pGB) via Golden Gate approach by the Vienna BioCenter Core Facilities (VBCF) Protech Facility. To express mCherry labelled PI3K complex 1 L culture of Sf9 cells growing in Sf921 medium at 1-1.5 mil/ml cells/volume were infected with 1 ml of Virus 1 (V1). Baculovirus was obtained by transfection of Sf9 cells with a policystronic construct coding for the mCherry labelled PI3K complex (Table S2). After infection cells were monitored and harvested by centrifugation when they reached a viability of 95-98%. Cell pellets were washed with PBS, flash frozen in liquid nitrogen, and stored at -80 °C until purification. To purify mCherry labelled PI3K complex the cell pellet corresponding to 1L culture was thawed and resuspended in 50 ml lysis buffer (50 mM HEPES pH 7.5, 300 mM NaCl, 0.5 % CHAPS, Benzonase, 1 mM $MgCl_2$, 1 mM DTT, CIP protease inhibitor (Sigma), cOmplete EDTA-free protease inhibitor cocktail (Roche). Cells were additionally disrupted with Dounce homogenizer. Lysates were cleared by centrifugation at 25 000 rpm for 45 min at 4°C in a Ti45 rotor (Beckman). Supernatant was incubated with 5 ml of Glutathione Sepharose 4B beads slurry (Cytiva) for 1h at 4°C. Then beads were washed twice with 50 mM HEPES pH 7.5, 30 0mM NaCl, 0.5% CHAPS, 1 mM DTT, twice with 50 mM HEPES pH 7.5, 700 mM NaCl, 1 mM DTT and finally twice with 50 mM HEPES pH 7.5, 300 mM NaCl, 1 mM DTT. To elute the protein complex

the beads were incubated overnight with Precission (3C) protease at 4°C. The supernatant containing cleaved protein was filtered through a 0.2 μm syringe filter, concentrated down to 0.5 ml and applied onto a Superose 6 column (10/300, Cytiva) pre-equillibrated with a buffer containing 50 mM HEPES pH 7.5, 200 mM NaCl, 1 mM DTT. Fractions containing pure proteins were pooled, concentrated, snap frozen in liquid nitrogen, and stored at −80°C. The protocol is available at https://doi.org/10.17504/protocols.io.8epv59mz4g1b/v1.

Microscopy-based bead protein-protein interaction assay

Glutathione Sepharose 4B beads (GE Healthcare), RFP- or GFP-Trap beads (ChromoTek), were mixed with GST, mCherry or GFP tagged bait proteins, respectively to the final concentrations of 10 μM (GST-4xUb), 2.5 μM (GFP-TBK1) and 1 μM (PI3Kc1-mCh). Beads were incubated with bait proteins at 4 °C for 1 h, and then washed twice with washing buffer (25mM TRIS-Cl pH 7.5, 150mM NaCl, 1mM DTT). 1 μl of respective beads was transferred into the well of a 384-well glass-bottom microplate (Greiner Bio-One) pre-filled with 20 μl of 25mM TRIS-Cl pH 7.5, 150mM NaCl, 1mM DTT and prey proteins. For the experiments shown in Figure 2G, mCh-NDP52 and FIP200-GFP were used at the final concentration of 100 nM and 500 nM, respectively. For the experiments shown in Figures 6A and 6B, PI3Kc1-mCh and mCherry were used at the final concentration of 200 nM, GFP-TBK1 and OPTN S177D S473D at the final concentration of 500 nM. For the experiments shown in Figures 6C, S7A, and S7B, ULK1c-GFP, GFP and NDP52 were used at the final concentration of 500 nM, and PI3Kc1-mCh at the final concentration of 200 nM. For experiments shown in Figure S4D to coat GSH beads GST-OPTN and GST were used at the final concentration of 5 μM. The prey proteins were added at the final concentration of 0.4 μM. For experiments shown in Figures S5B and S5D the baits (GST-NDP52 and GST) were used at 5 μM. The prey proteins GFP-TBK1 and mCh-TBK1 were added at the final concentration of 0.1 uM, whereas NAP-mCh and SINTBAD-GFP at the final concentration of 0.3 μM. The samples were incubated for 30 min and imaged at the equilibrium by Zeiss LSM 700 confocal microscope equipped with Plan Apochromat 20X/0.8 WD 0.55 mm objective.

For quantification of mCh-NDP52 recruitment to the beads in the presence and absence of FIP200-GFP (Figure 2I) using ImageJ software eight lines were drawn across each bead and the maximum brightness value along each the line was taken. Next, the average brightness of an empty area of each picture was measured (background fluorescence) and subtracted from the maximal fluorescence for each bead. The average values for each sample were averaged between 3 independent replicates and plotted with the relative standard errors. For the quantification described above, statistical analysis was performed. Statistical significance of the difference between 2 samples was established by 2 samples unpaired t test. Significant differences are indicated with * when p value $\leq$ 0.05, ** when p value $\leq$ 0.01, *** when p value $\leq$ 0.001. The Protocol for this is available online (https://doi.org/10.17504/protocols.io.6qpvr6nwpvmk/v1)

In vitro kinase assay

For *in vitro* kinase assay, 50 nM of TBK1 or ULK1 complex (composed of ULK1, FIP200, ATG13, and ATG101) was incubated with 800 nM PI3K complex for indicated time points at room temperature in the kinase buffer (20 mM TRIS-Cl pH 7.4, 150 mM NaCl, 1 mM DTT, 10 mM $MgCl_2$, 0.1 mM ATP). To control for potential protein instability, all protein mixtures were kept at room temperature for the same amount of time. The kinase reaction was induced by adding 2x ATP/$MgCl_2$ kinase buffer, starting with the time point 30 min. All samples were inactivated by adding 6x protein loading sample buffer and boiling for 5 min at 95°C. Samples were separated by SDS-PAGE and analyzed by immunoblotting. For Mass spectrometry experiment (next section) the incubation time was 30 min. As a negative control, the same protein mixtures were incubated in a kinase buffer lacking $MgCl_2$ and ATP. Samples were separated by SDS-PAGE and stained with Coomassie. The bands for each subunit of the PI3K complex (VPS15, VPS34, ATG14, and Beclin1) were cut out from the gel and submitted for mass spectrometry analysis. Two independent assays were performed. The protocol for *in vitro* kinase assay is available online https://doi.org/10.17504/protocols.io.j8nlkwr51l5r/v1

Mass spectrometry analysis, data analysis and figure preparation

Mass spectrometry (MS) service was done by Max F. Perutz Mass Spectrometry Facility (University of Vienna, Austria) and the data and protocols can be found at ProteomeXchange Consortium via the PRIDE partner repository with the dataset identifier PXD039663.

The Coomassie-stained gel band was destained with a mixture of acetonitrile (Chromasolv®, Sigma-Aldrich) and 50 mM ammonium bicarbonate (Sigma-Aldrich). The proteins were reduced using 10 mM dithiothreitol (Roche) and alkylated with 50 mM iodoacetamide. Digestion was carried out with trypsin (Promega; Trypsin Gold, Mass Spectrometry Grade) at 37°C overnight. Formic acid was used to stop the digestion and extract peptides.

Peptides were separated on an Ultimate 3000 RSLC nano-flow chromatography system (Thermo-Fisher), using a pre-column for sample loading (Acclaim PepMap C18, 2 cm × 0.1 mm, 5 μm, Thermo-Fisher), and a C18 analytical column (Acclaim PepMap C18, 50 cm × 0.75 mm, 2 μm, Thermo-Fisher), applying a segmented linear gradient from 2% to 35% and finally 80% solvent B (80 % acetonitrile, 0.1 % formic acid; solvent A 0.1 % formic acid) at a flow rate of 230 nL/min over 60 min.

Eluting peptides were analyzed on a Q Exactive HF-X Orbitrap mass spectrometer (Thermo Fisher), which was coupled to the column with a customized nano-spray EASY-Spray ion-source (Thermo-Fisher) using coated emitter tips (New Objective). The mass spectrometer was operated in data-dependent acquisition mode (DDA), and survey scans were obtained in a mass range of 375-1500 m/z with lock mass activated, at a resolution of 60k at 200 m/z and an AGC target value of 3E6. The 15 most intense ions

were selected with an isolation width of 1.2 m/z, fragmented in the HCD cell at 28% collision energy, and the spectra recorded for max. 100 ms at a target value of 1E5 and a resolution of 30k. Peptides with a charge of +1 or >+6 were excluded from fragmentation, the peptide match feature was set to preferred, the exclude isotope feature was enabled, and selected precursors were dynamically excluded from repeated sampling for 20 seconds.

Raw data were processed using the MaxQuant software package (version 2.0.3.0),[101] and target proteins sequences, the Uniprot Spodoptera frugiperda reference proteome (version 2021.04, www.uniprot.org) as well as a database of most common contaminants. The search was performed with full trypsin specificity and a maximum of three missed cleavages at a protein and peptide spectrum match false discovery rate of 1%. Carbamidomethylation of cysteine residues was set as fixed, oxidation of methionine, phosphorylation of serine, threonine, and tyrosine, and N-terminal acetylation as variable modifications. For label-free quantification the ''match between runs'' feature and the LFQ function were activated - all other parameters were left at default.

Peptide intensity datasets were analysed using R (Ver.>4.2). Peptides were excluded if they had no detection in any sample. If the score of the peptide was also below 90 the peptide was excluded. All peptides with a score between 90 and 100 were noted with a low score but used in the analysis. To show the relative phosphorylation, peptide intensity at time point 0 was subtracted from the respective 30 minute time point for all samples. Proteins were plotted if they were detected in their appropriate band when cutting the western blot. Code analysis in RMarkdown as well as the trimmed csv file and pdf export can be found in the listed Github Repository (Shoebridge 2023).

Stephen Shoebridge. (2023). shoebridges/asap_phosphosites: Preview Release (Pre-Release). Zenodo. https://doi.org/10.5281/zenodo.7576089

QUANTIFICATION AND STATISTICAL ANALYSIS

For western blots, band intensities were measured with ImageLab (BioRad). All statistical analyses were performed using GraphPad Prism. Statistical significance was calculated from three independent experiments using one-way or two-way ANOVA or Student's t test as specified in figure legends with a confidence interval of 95%. Error bars are reported as mean ± standard deviation.